NASA Contractor Report 4440

A Compressible Navier-Stokes Solver With Two-Equation and Reynolds Stress Turbulence Closure Models

Joseph H. Morrison

NASA

NASA Contractor Report 4440

A Compressible Navier-Stokes Solver With Two-Equation and Reynolds Stress Turbulence Closure Models

Joseph H. Morrison
Analytical Services & Materials, Inc.
Hampton, Virginia

NASA

National Aeronautics and
Space Administration

Office of Management

Scientific and Technical
Information Program

1992
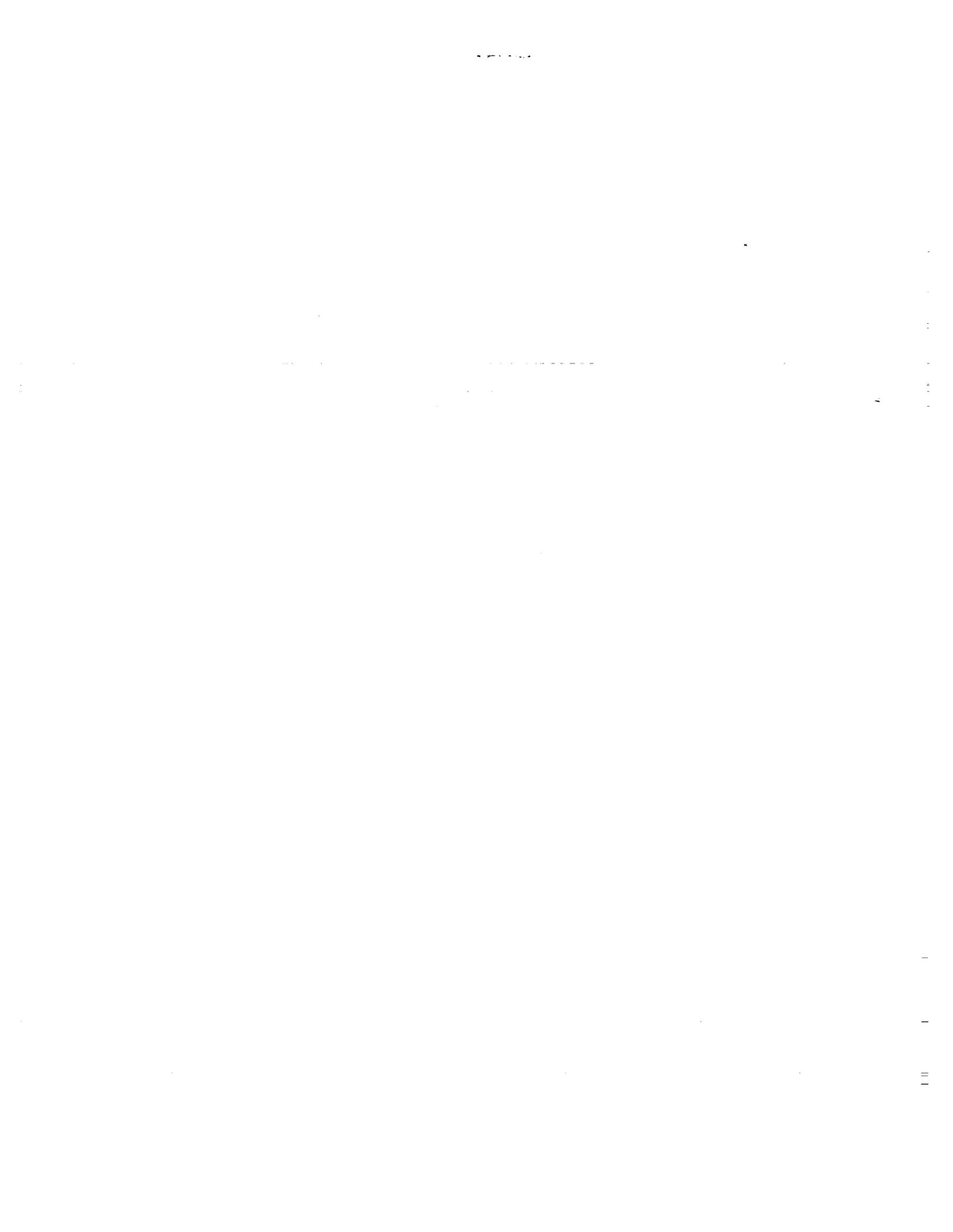
A COMPRESSIBLE NAVIER-STOKES SOLVER WITH TWO-EQUATION AND REYNOLDS STRESS TURBULENCE CLOSURE MODELS

Joseph H. Morrison

Analytical Services & Materials, Inc.
107 Research Drive, Hampton, VA 23666

ABSTRACT

This report outlines the development of a general purpose aerodynamic solver for compressible turbulent flows. Turbulent closure is achieved using either two-equation or Reynolds stress transport equations. The applicable equation set consists of Favre-averaged conservation equations for the mass, momentum and total energy, and transport equations for the turbulent stresses and turbulent dissipation rate. In order to develop a scheme with good shock-capturing capabilities, good accuracy and general geometric capabilities, a multi-block, cell-centered finite-volume approach is used. A Roe flux-difference splitting technique, coupled with a MUSCL scheme, is applied to the system of conservation and transport equations. Viscous fluxes are discretized using a finite-volume representation of a central-difference operator and the source terms are treated as an integral over the control-volume. The methodology is validated by testing the algorithm on both two-dimensional and three-dimensional flows. Both the two-equation and Reynolds stress models are used on a two-dimensional 10° compression ramp at Mach 3, and the two-equation model is used on the three-dimensional flow over a cone at angle of attack at Mach 3.5. With the development of this algorithm, it is now possible to compute complex, compressible high-speed flow fields using both two-equation and Reynolds stress turbulent closure models, with the capability of eventually evaluating their predictive performance.

1

1 Introduction

There has been an increasing desire to predict the turbulent flow behavior over complicated aerodynamic geometries in both low- and high-speed flows. This goal will certainly lie outside the scope of direct numerical simulations (DNS) and even large eddy simulations (LES) in the near future [1], even with anticipated increases in computational speed. Thus practical computations will necessarily rely on the utilization of phenomenological models for the turbulent transport equations. Until recently, work in these areas was further limited to the incompressible regime with relatively little focused research in the compressible area [2]. In the incompressible regime, there has been significant progress in the area of predictive solutions for turbulent flows in a wide variety of cases to date. In the more complex flow situations, the simpler turbulence models can be readily implemented and these have been used most extensively. Their success has been measured by their performance in generating mean flows and wall pressures, which are not strongly dependent on the correct modeling of turbulent transport properties. However, the complex flows where turbulent transport is important require more sophisticated turbulence models in order to capture the underlying physics.

It is only with the initiation of such national priority efforts as the National Aero-Space Plane (NASP) and the High-Speed Civil Transport (HSCT) that there has been a strong impetus into the compressible regime for these turbulent stress closure models. Unfortunately, the practical aerodynamic flows that we are ultimately interested in are three dimensional with strong vortical regions and generally far from equilibrium. As has already been noted, such fully three-dimensional flows cannot be adequately predicted using simple eddy viscosity type models because of the strong anisotropies in the flow. It is necessary to increase the physics within the turbulent transport models, and this can be done by advancing to Reynolds stress transport models. While these models contain improved capabilities for the stress anisotropies and the associated strain histories, their computational stiffness has lessoned their appeal to the general user community. These stiffness problems can be traced to the near-wall corrections applied to the high Reynolds number versions of the transport models. For this reason, wall function corrections have proved useful since they can remove the stiffness problems; however, this is done at the expense of constraining the Reynolds stress transport models to attached flows.

The task at hand is to develop a versatile means of implementing Reynolds stress transport models into generally applicable aerodynamic codes for application to high-speed compressible flows. This task, while straightforward in concept, is practically very cumbersome because of the significant number of terms in the turbulent transport equations and the nonlinear coupling between the mean flow equations and the transport equations. Add to this the unknown correlations resulting from the compressibilty of the flow and one can see that it is a challenging task to effectively develop a robust computational tool for studying complex compressible flows using

Reynolds stress turbulence models.

Mean conservation and transport equations used in the solution of compressible turbulent flows are presented in Section 2. These include the conservation of mean mass, momentum and energy, as well as the transport equations for the various turbulent Reynolds stresses and turbulent dissipation rate. The models for the unknown turbulent correlations in the high Reynolds number form of these equations are also presented. The corrections to these models to account for the near-wall effects of solid boundaries is discussed separately in Section 3. In Section 4, the 12 partial differential equations (7 for the two-equation model) comprising the solution set are recast in vector form. The dependent variable vector includes the density, velocities, total energy, turbulent Reynolds stresses and dissipation rate. The discretization of the resulting inhomogeneous flux equation, expressed in generalized coordinates, is then discussed.

In the context of the present report where the intent is to establish the differential and numerical framework for the solution of the equations, it is not advantageous to do a detailed predictive study of particular compressible flows. It is necessary, however, to compute some representative flow fields in order to validate the capabilities of the numerical code. Detailed comparisons will require the choice of a more accurate near-wall model for the Reynolds stress formulation. The two flows that will be considered here are the two-dimensional compression ramp and the three-dimensional cone. For the ramp problem, the flow is computed using both the two-equation and Reynolds stress models, and for the cone problem only the two-equation model is used. The results from the calculations are given in Section 5 where profiles at selected streamwise (ramp) or azimuthal (cone) stations are shown for both the mean and turbulent quantities.

2 Conservation and Transport Equations

It has been known for some time that the optimal way, both mathematically and physically, of formulating both the mean conservation equations and the Reynolds stress transport equations is to employ Favre or mass-weighted averages [3, 4]. This is due to the resulting similarity between the incompressible and compressible form of the equations. For completeness, the relevant mean conservation and Reynolds stress transport equations are given here. Any dependent flow variable f can be decomposed using the usual Reynolds decomposition given by

$$f = \overline{f} + f',$$
(2.1)

where

$$\overline{f} = \lim_{\tau \to \infty} \frac{1}{\tau} \int_0^\tau f(\mathbf{x}, t)\, dt$$

or a Favre-average given by

$$f = \tilde{f} + f'',$$
(2.2)

where

$$\tilde{f} = \frac{\overline{\rho f}}{\overline{\rho}}.$$
(2.2a)

In the equation development that follows, the dependent variables are the density ρ, the pressure p, the temperature T, the velocity u_i, the turbulent Reynolds stress τ_{ij} and the turbulent dissipation rate ϵ_{ij}. The differential equations are written in Cartesian tensor notation for compactness and consistency. In the following derivations, the "$=$" sign for the unknown correlations means the exact functional form, and the "$\simeq$" sign means the modeled or approximate form.

2.1 Conservation Equations

The mean conservation equations for mass, momentum and total energy can then be written as

MASS

$$\partial_t \overline{\rho} + (\overline{\rho} \tilde{u}_k)_{,k} = 0$$
(2.3)

MOMENTUM

$$\partial_t (\overline{\rho} \tilde{u}_i) + (\overline{\rho} \tilde{u}_i \tilde{u}_j + \overline{p} \delta_{ij})_{,j} = \overline{\sigma}_{ij,j} - (\overline{\rho} \tau_{ij})_{,j}$$
(2.4)

where

$$\overline{\sigma}_{ij} = -\frac{2}{3} \overline{\mu u_{k,k}} \delta_{ij} + \overline{\mu(u_{i,j} + u_{j,i})}$$

4

$$\simeq -\frac{2}{3}\overline{\mu}\tilde{u}_{k,k}\delta_{ij} + \overline{\mu}(\tilde{u}_{i,j} + \tilde{u}_{j,i}) \tag{2.4a}$$

is the viscous stress tensor with $\overline{\mu}$ the mean molecular viscosity calculated from Sutherland's law.

TOTAL ENERGY

$$\partial_t(\overline{\rho}\tilde{E}) + [\tilde{u}_j(\overline{\rho}\tilde{E} + \overline{p})]_{,j} = (\overline{\sigma}_{ij}\tilde{u}_i + \overline{\sigma_{ij}u_i''} - \overline{q}_j)_{,j} + (\overline{\sigma_{ij}'u_i'} - \overline{\rho E''u_j''})_{,j} \tag{2.5}$$

where

$$\tilde{E} = c_v\tilde{T} + \frac{\tilde{u}_i\tilde{u}_i}{2} + \frac{\widetilde{u_i''u_i''}}{2} \tag{2.5a}$$

$$\overline{q}_j = -\overline{\kappa T_{,j}}$$

$$\simeq -\overline{\kappa}\tilde{T}_{,j} \tag{2.5b}$$

$$\overline{\rho E''u_j''} = C_v\overline{\rho u_j''T''} + \overline{\rho}\tilde{u}_i\tau_{ij} + \frac{\overline{\rho u_i''u_i''u_j''}}{2}, \tag{2.5c}$$

$\overline{q}_j$ is the mean heat flux vector, and $\overline{\kappa}$ is the mean thermal conductivity. The energy equation is written in terms of the total energy because this formulation is necessary in order to effectively employ shock capturing techniques in the numerical solution algorithm [5].

2.2 Transport Equations

Equation (2.4) contains the Favre-averaged Reynolds stress tensor, $(\tau_{ij} \equiv \widetilde{u_i''u_j''})$. In the utilization of a two-equation closure, the individual stress components are obtained by way of a Boussinesq approximation relating the turbulent stresses to mean velocity gradients,

$$\overline{\rho}\tau_{ij} \simeq \frac{2}{3}\overline{\rho}k\delta_{ij} - 2\overline{\mu}_t\left[\tilde{S}_{ij} - \frac{2}{3}\tilde{S}_{kk}\right] \tag{2.6}$$

with the eddy viscosity given by

$$\overline{\mu}_t = C_\mu\overline{\rho}\frac{k^2}{\epsilon}, \tag{2.6a}$$

where $\tilde{S}_{ij}(= (\tilde{u}_{i,j} + \tilde{u}_{j,i})/2)$ is the strain rate tensor, and C_μ a constant usually taken to be (0.09). This type of closure is clearly inaccurate in regions close to solid boundaries, since it assumes an isotropic distribution of the stresses with respect to the kinetic energy. This is easily demonstrated by recalling that in the near-wall region asymptotic analyses [6] show that while the streamwise and spanwise normal stresses behave as the kinetic energy (i.e. as $\mathcal{O}(y^2)$, where y is the distance normal to the wall), the transverse normal stress τ_{yy} goes as $\mathcal{O}(y^4)$. A near-wall correction is clearly

5

needed and this will be the topic of discussion in the next section for both the two-equation and Reynolds stress models. Nevertheless, this two-equation approach is quite useful since it couples the turbulent kinetic energy equation with an appropriate scale equation so that there are only two transport equations which need to be solved.

The Reynolds stress transport equation approach solves transport equations for the individual stress components as well as an appropriate scale equation. While the deficiencies with the use of the Boussinesq approximation are removed, they are replaced with the complicating factor of needing to solve six transport equations for the various stress components (the Reynolds stress tensor being symmetric for flows of interest in aerodynamic flight). The incorporation of the Reynolds stress formulation within a general Navier-Stokes solver is intended to ultimately serve as a means of comparison with the two-equation formulation.

Since the turbulent kinetic energy equation is simply the contraction of the full Reynolds stress transport equation, it suffices to outline the modeling of the Reynolds stress transport equation and point out any differences that may result.

REYNOLDS STRESS TRANSPORT

$$\partial_t(\overline{\rho}\tau_{ij}) + (\tilde{u}_k\overline{\rho}\tau_{ij})_{,k} = P_{ij} + \Pi_{ij}^d + \Pi_{ij}^{dl} + M_{ij} + D_{ij}^v + D_{ij}^t - \overline{\rho}\epsilon_{ij} \quad (2.7)$$

where the right hand side represents the turbulent stress transport produced by the turbulent production, P_{ij}, the deviatoric part of the pressure strain-rate correlation, Π_{ij}^d, the pressure dilatation, Π_{ij}^{dl}, the mass flux variation, M_{ij}, the viscous diffusion, D_{ij}^v, the turbulent diffusion, D_{ij}^t, and the turbulent dissipation rate. These terms are given by

$$P_{ij} = -\overline{\rho}\tau_{ik}\tilde{u}_{j,k} - \overline{\rho}\tau_{jk}\tilde{u}_{i,k} \quad (2.7a)$$

$$\Pi_{ij}^d = \overline{p'u'_{i,j}} + \overline{p'u'_{j,i}} - \frac{2}{3}\overline{p'u'_{k,k}}\delta_{ij} \quad (2.7b)$$

$$\Pi_{ij}^{dl} = \frac{2}{3}\overline{p'u'_{k,k}}\delta_{ij} \quad (2.7c)$$

$$M_{ij} = \overline{u''_i}(\overline{\sigma}_{jk,k} + \overline{\sigma}_{ik,k} - \overline{p}_{,j} - \overline{p}_{,i}) \quad (2.7d)$$

$$D_{ij}^v = (\overline{\sigma'_{ik}u'_j + \sigma'_{jk}u'_i})_{,k} \quad (2.7e)$$

$$D_{ij}^t = -[\overline{\rho u''_i u''_j u''_k} + (\overline{p'u'_i}\delta_{jk} + \overline{p'u'_j}\delta_{ik})]_{,k} \quad (2.7f)$$

$$\epsilon_{ij} = \overline{\sigma'_{ik}u'_{j,k}} + \overline{\sigma'_{jk}u'_{i,k}}. \quad (2.7g)$$

The general form of the turbulent kinetic energy equation is obtained from Eq. (2.7) using the definition $k = \tau_{ii}/2$.

The remaining transport equation that is used in both two-equation and Reynolds stress closures adopted here is the turbulent dissipation rate equation. Using the

defining relationship shown in Eq. (2.7g), it is derivable from the fluctuating momentum equation. As in the incompressible case (e.g. [7]), this equation is quite complex and there is no direct experimental evidence about any of the terms in the equation. The approach that has been taken to date in the development of a dissipation rate model that can be used in compressible flows is to partition the dissipation rate into a solenoidal (incompressible) component and a compressible component [8, 9]. Compressibility effects are then represented as asymptotic corrections to the incompressible (solenoidal) dissipation rate. This allows for the direct utilization of the incompressible form of the dissipation rate transport equation. The form of the dissipation rate partitioning that is adopted in the present work is given by [9]

$$\epsilon = \epsilon_s + \epsilon_c$$
$$\simeq \epsilon_s(1 + \alpha_1 M_t^2) \tag{2.8}$$

where $\alpha_1 (= 0.6)$ is a numerical constant extracted from comparisons with direct simulation data [2], and $M_t (= \sqrt{\tau_{ii}}/\bar{a}_\infty)$ is the turbulent Mach number. A general high Reynolds number form of the isotropic solenoidal dissipation rate equation has been derived [10].

DISSIPATION RATE EQUATION

$$\partial_t(\bar{\rho}\epsilon_s) + (\tilde{u}_k\bar{\rho}\epsilon_s)_{,k} = -\frac{4}{3}\bar{\rho}\epsilon_s\tilde{u}_{i,i} + \bar{\rho}\epsilon_s\frac{1}{\bar{\nu}}\frac{D\bar{\nu}}{Dt} + P_{\epsilon_s} - \mathcal{D}_{\epsilon_s} + D^t_{\epsilon_s} + D^v_{\epsilon_s} \tag{2.9}$$

where P_{ϵ_s} is the production, $\mathcal{D}_{\epsilon_s}$ is the destruction, $D^t_{\epsilon_s}$ is the turbulent diffusion, and $D^v_{\epsilon_s}$ is the viscous diffusion.

2.3 Higher-Order Correlation Models

As can be seen from an examination of the compressible mean conservation and turbulent transport equations, there are several higher order correlations which need to be modeled. In the incompressible regime, several of these terms have well established models which have been tested and proven in a variety of flow situations. The modeling of the unknown correlations in the compressible case is not as mature so there are more uncertainties in the predictive capabilities of these equations. Since this is a very active research area at the present time, the focus of the present report is to develop the numerical techniques for a rather general form of the equations. As new models are developed, they then can be easily implemented into the existing numerical structure.

In the equation for the total energy, Eq. (2.5), both the viscous diffusion and the energy flux need to be modeled. The viscous diffusion term that appears in the total energy equation is the contraction of the corresponding term in the Reynolds stress transport equation, Eq. (2.7e). In the solution of the Reynolds stress transport equations in incompressible high Reynolds number flows, this term is frequently neglected

7

since it is usually dominated by turbulent diffusion effects. When it is taken into account, it is usually treated simply in its gradient diffusion form and is written as

$$\overline{\sigma'_{ik}u'_j + \sigma'_{jk}u'_i} \simeq \bar{\mu}(\tau_{ij,k} + \tau_{jk,i} + \tau_{ik,j}). \tag{2.10}$$

The contraction of Eq. (2.10) leads to the appropriate model for the viscous diffusion term in the total energy equation.

The energy flux term, Eq. (2.5c), requires models for both the heat flux and triple velocity correlation terms. At present there has not been any consistent effort to develop alternatives to the gradient diffusion hypothesis for the heat flux term. For simplicity, the heat flux term is then modeled as

$$\overline{\rho u''_j T''} \simeq -\bar{\kappa}_t \tilde{T}_{,j} \tag{2.11}$$

where $\bar{\kappa}_t$ is the thermal eddy diffusivity which is given here as (cf. Eq. (2.6a)),

$$\bar{\kappa}_t = C_\mu \frac{\bar{\rho}k^2}{\mathrm{Pr}_t\,\epsilon_s} = \frac{\bar{\mu}_t}{\mathrm{Pr}_t}. \tag{2.12}$$

As is seen by the form of Eq. (2.12), the thermal eddy diffusivity used here is simply the usual eddy viscosity divided by the turbulent Prandtl number $\mathrm{Pr}_t(= 0.9)$.

The remaining contribution in the energy flux term is the triple correlation or the turbulent diffusion term. This term is also present in the Reynolds stress equation in its uncontracted form (cf. Eq. (2.7f). This term has also been traditionally modeled with a gradient diffusion hypothesis by using a turbulent eddy viscosity. The form adopted here is given by

$$\overline{\rho u''_i u''_j u''_k} \simeq -\frac{2}{3}C_s \frac{\bar{\rho}k^2}{\epsilon_s}(\tau_{ij,k} + \tau_{jk,i} + \tau_{ik,j}) \tag{2.13}$$

where C_s is a numerical constant which is assigned the value of 0.18. This is an isotropized version of the model used by Launder, Reece, and Rodi [11]. In their model, the coefficient C_s was chosen to be 0.11, but in its present form the higher value used here is more appropriate. This model incorporates the functional form of the eddy viscosity relationship defined previously but with a different proportionality coefficient, $\bar{\mu}_t/\sigma_k$, with $\sigma_k = 0.75$. Contraction of Eq. (2.13) will lead to the required functional form used in the energy flux model.

The models required for closure of the total energy equation have now been identified and it is necessary to examine the remaining unknown correlations in the Reynolds stress transport equations. The mass flux variation appearing in the Reynolds stress transport equation is represented by Eq. (2.7d). Consistent with the other correlations which are unique to the compressible formulation, the mass flux term is also modeled by invoking the gradient diffusion hypothesis;

$$\overline{u''_i} \simeq \frac{C_\mu}{\bar{\rho}\sigma_\rho} \frac{k^2}{\epsilon_s}\bar{p}_{,i} = \frac{\bar{\mu}_t}{\bar{\rho}^2\sigma_\rho}\bar{p}_{,i} \tag{2.14}$$

8

where σ_ρ is a constant whose value is 0.5.

The modeling of the pressure dilatation term has been the subject of analysis following the partitioning ideas invoked earlier for the dissipation rate term [12, 13]. The form proposed in [12] is used here and is given by

$$\overline{p'u'}_{k,k} \simeq \bar{p}M_t^2(\alpha_2\tau_{ij}\tilde{u}_{i,j} + \alpha_3\epsilon_s) \tag{2.15}$$

where $\alpha_2(= 0.6)$ and $\alpha_3(= 0.2)$ are numerical constants calibrated by comparison with direct numerical simulations [12].

The only remaining model that needs to be determined is for the deviatoric part of the pressure-strain rate correlation, Eq. (2.7b). At present there has been no work directed toward the development of a compressible pressure-strain rate correlation model. The approach taken has been to use variable density extensions of the incompressible form of the model. The compressibility effects have then been isolated into the pressure dilatation term which has been solely derived for compressible flows. In light of this approach and the fact that there are a significant number of pressure-strain rate models presented in the literature, it is sufficient in the present context to present the functional form of a commonly used model and show its incorporation into the numerical algorithm. One of the most commonly used pressure-strain rate correlation models is the model of Launder, Reece and Rodi [11]. While it is only linear in the anisotropies of the Reynolds stress, it has been used extensively on a variety of flows. The high Reynolds number form of the equation is given by

$$\Pi_{ij}^d \simeq \phi_{ij1} + \phi_{ij2} \tag{2.16}$$

$$\phi_{ij1} = -C_1\bar{p}\epsilon b_{ij} \tag{2.16a}$$

$$\phi_{ij2} = -\frac{C_2+8}{11}(P_{ij} - \frac{1}{3}P_{kk}\delta_{ij}) - \frac{8C_2-2}{11}(D_{ij} - \frac{1}{3}P_{kk}\delta_{ij})$$
$$- \frac{30C_2-2}{55}\bar{p}k(\tilde{u}_{i,j} + \tilde{u}_{j,i} - \frac{2}{3}\tilde{u}_{k,k}\delta_{ij}) \tag{2.16b}$$

where C_1 and C_2 are numerical constants given by 3.0 and 0.4, respectively, and

$$b_{ij} = \frac{1}{2k}(\tau_{ij} - \frac{2}{3}k\delta_{ij}) \tag{2.17a}$$

$$D_{ij} = -\bar{p}\tau_{ik}\tilde{u}_{k,j} - \bar{p}\tau_{jk}\tilde{u}_{k,i} \tag{2.17b}$$

It should be emphasized that the pressure-strain rate correlation is the subject of extensive research and that other models have been proposed which should perform better than the above model (e.g. [14]). However, comparing a variety of closure models is not the intent of the present report, but is a course of study being actively pursued and will be reported on later.

The remaining equation that needs to be modeled is the solenoidal dissipation rate equation, Eq. (2.9). This equation has been examined recently [15, 10] for application to compressible flows. The models for the terms in Eq. (2.9) are given by

9

$$\frac{1}{\bar{\nu}}\frac{D\bar{\nu}}{Dt} = [1 - m(\gamma - 1)]\tilde{u}_{i,i} \tag{2.18a}$$

$$P_{\epsilon_s} = -C_{\epsilon 1}\frac{\epsilon_s}{k}\bar{\rho}\tau_{ij}(\tilde{u}_{i,j} - \frac{1}{3}\tilde{u}_{k,k}\delta_{ij}) \tag{2.18b}$$

$$\mathcal{D}_{\epsilon_s} = C_{\epsilon 2}\bar{\rho}\frac{\epsilon_s^2}{k} \tag{2.18c}$$

$$D_{\epsilon_s}^t = C_\epsilon\left(\frac{\bar{\rho}k}{\epsilon_s}\tau_{kl}\epsilon_{s,l}\right)_{,k} \tag{2.18d}$$

$$D_{\epsilon_s}^v = (\bar{\mu}\epsilon_{s,k})_{,k} \tag{2.18e}$$

where $C_{\epsilon 1}, C_{\epsilon 2}$ and C_ϵ are modeling coefficients which take the values $1.50, 1.83$ and 0.15, respectively, γ is the ratio of specific heats $(= 1.4)$, and $m(\approx 0.7)$ is the exponent of a power law approximation for the mean molecular viscosity [16].

Equation (2.9) can then be rewritten as

$$\partial_t(\bar{\rho}\epsilon_s) + (\bar{\rho}\tilde{u}_k\epsilon_s)_{,k} = -[\frac{1}{3} + m(\gamma - 1)]\bar{\rho}\epsilon_s\tilde{u}_{i,i} - C_{\epsilon 1}\frac{\epsilon_s}{k}\bar{\rho}\tau_{ij}(\tilde{u}_{i,j} - \frac{1}{3}\tilde{u}_{k,k}\delta_{ij})$$

$$-C_{\epsilon 2}\bar{\rho}\frac{\epsilon_s^2}{k} + C_\epsilon\left(\frac{\bar{\rho}k}{\epsilon_s}\tau_{kl}\epsilon_{s,l}\right)_{,k} + (\bar{\mu}\epsilon_{s,k})_{,k} \tag{2.19}$$

This now completes the specification of the transport equations and closure models needed for the solution of turbulent flows. The models presented up to this point have been high Reynolds number models, that is, models applicable to flows away from walls. In the presence of solid boundaries, the desire is to integrate directly to the wall so that wall functions do not have to be implemented. While the use of wall functions reduces the stiffness of the equation set, it constrains the application of the models to attached flows. Integrating directly to the wall requires near-wall modifications to the models already presented. For clarity, these near-wall modifications will be discussed in the next section for both the two-equation and Reynolds stress models.

3   Near-Wall Corrections

The equation sets presented in the previous section outlined the high Reynolds number form of the equations. In the presence of solid boundaries, these equations need to be modified to account for the low Reynolds number flow near the solid surface. This area has received considerable attention in the incompressible regime (e.g. [17, 18]) while in the compressible regime work is only beginning [10]. Due to the uncertainty in developing such near-wall models at this point, it suffices here to show the types of modifications that are incorporated into the high Reynolds number models of the previous section.

As was alluded to in the previous section, the two-equation turbulence models suffer from inaccurate distribution of Reynolds stress values in the vicinity of walls. This inaccuracy is accounted for by introducing a wall damping function into the defining relationship for the eddy viscosity, Eq. (2.6a). The modified near-wall form is

$$\bar{\mu}_t = C_\mu f_\mu \bar{\rho} \frac{k^2}{\epsilon},$$
(3.1)

where the damping function f_μ is given by

$$f_\mu = \left(1 + \frac{3.45}{\sqrt{Re_t}}\right)\left[1 - \tanh\left(-\frac{y^+}{70}\right)\right]$$
(3.2)

where y^+ is the distance normal to the wall in wall variables, and Re_t is the turbulent Reynolds number defined as $k^2/\bar{\nu}\epsilon_s$. Note that far from the wall the value of f_μ is delimited by unity to consistently merge with the high Reynolds number form of the models. This analytic representation for f_μ is by no means unique; however, comparison with direct simulation results [19] in incompressible boundary-layer flow has shown this to be a reasonable representation of the correct near-wall behavior. Note that it also carries over to the subsequent implementation of the eddy viscosity in the other closure approximation of the previous section. This includes the triple correlation model used in Eq. (2.13) which now becomes

$$\overline{\rho u_i'' \widetilde{u_j'' u_k''}} \simeq -\frac{2}{3}\bar{\rho} C_s f_\mu \frac{k^2}{\epsilon_s}(\tau_{ij,k} + \tau_{jk,i} + \tau_{ik,j}).$$
(3.3)

or, for the two-equation model

$$\frac{1}{2}\overline{\rho u_i'' \widetilde{u_i'' u_k''}} \simeq -\frac{\bar{\mu}_t}{\sigma_k}(k_{,k} + \tau_{ik,i}).$$
(3.4)

where $\sigma_k = 0.75$.

The remaining term that needs to be modified in the equations to account for the presence of solid boundaries is the destruction term, $\mathcal{D}_{\epsilon_s}$, in the solenoidal disspation rate equation. This term is then rewritten as

11

$$\mathcal{D}_{\epsilon_s} = C_{\epsilon 2} f_2 \overline{\rho} \frac{\epsilon_s^2}{k}, \tag{3.5}$$

where [6]

$$f_2 = \left[1 - \exp\left(\frac{y^+}{4.9}\right) \right]^2 \left[1 - \frac{2}{9} \exp\left(-\frac{Re_t^2}{36}\right) \right] \tag{3.6}$$

Note that in the absence of f_2 the destruction term increases without bound as the wall is approached.

For the Reynolds stress closure, a near-wall correction needs to be used for the pressure-strain rate correlation. This has been the topic of research in wall-bounded incompressible flows for some time [18], but with mixed success. Nevertheless, since the intent here is not to validate or compare models, it suffices to implement a near-wall correction which typifies the form and structure of a near-wall closure that can be implemented in the present numerical formulation. The near-wall modification that is adopted here is a variable density extension of the Shima model [20]. Even though this model has deficiencies which will be pointed out shortly, it is readily amenable to implementation in complex flows because it lacks any dependency on the wall normals [21] which cause ambiguities in complex flow situations. The Shima model introduces a near-wall correction to the pressure-strain correlation given by

$$\Pi_{ij} \simeq \phi_{ij1}^* + \phi_{ij2} + \phi_{ijw} \tag{3.7}$$

where

$$\phi_{ij1}^* \simeq -C_1^* \overline{\rho} \epsilon b_{ij} \tag{3.8}$$

with

$$C_1^* = C_1 + (1 - C_1) f_w \tag{3.8a}$$

$$f_w = \exp\left[-(0.015\sqrt{k} y/\overline{\nu})^4\right], \tag{3.8b}$$

ϕ_{ij2} given by Eq. (2.16b), and $C_1 = 3.0$. The coordinate y is measured normal to the surface. The near-wall correction ϕ_{ijw} is given by

$$\phi_{ij2} = [\alpha(P_{ij} - \frac{1}{3}P_{kk}\delta_{ij}) + \beta\overline{\rho}k(\tilde{u}_{i,j} + \tilde{u}_{j,i} - \frac{2}{3}\tilde{u}_{k,k}\delta_{ij})]f_w, \tag{3.9}$$

where $\alpha = 0.45$ and $\beta = 0.08$.

A near-wall correction to the solenoidal dissipation rate needs to be implemented. For consisitency, the model proposed by Shima [20] is again used in the present study. The solenoidal dissipation rate equation is easily modified to include the near-wall Shima correction by replacing $C_{\epsilon 1}$ with a $C_{\epsilon 1}^*$ defined as

$$C_{\epsilon 1}^* = C_{\epsilon 1}(1 + f_w), \tag{3.10}$$

12

and adding

$$D_{\epsilon_s}^w = \left\{ \left(-2 + \frac{7}{9} C_{\epsilon 2} \right) \frac{\epsilon_s \tilde{\epsilon}_s}{k} - \frac{\tilde{\epsilon}_s^2}{2k} \right\} f_w \qquad (3.11)$$

where

$$\tilde{\epsilon}_s = \epsilon_s - \bar{\nu} \frac{\partial^2 k}{\partial x_l \partial x_l} \qquad (3.11a)$$

to the right hand side of Eq. (2.19). With the introduction of the near-wall model, the closure coefficients $C_{\epsilon 1}, C_{\epsilon 2}$ and C_ϵ are given by $1.35, 1.80$ and 0.15, respectively, and f_w is given by Eq. (3.8b). Since the destruction term, $\mathcal{D}_{\epsilon_s}$, in the Shima model does not include any near-wall damping effect ($f_2 = 1$, cf. Eq. (3.5)), it is readily apparent that the destruction term in the solenoidal dissipation rate equation increases unbounded as the wall is approached. The effect of this deficiency becomes more pronounced as the grid resolution is increased and, therefore, needs to be corrected for quantitative comparisons.

The true test of these near-wall corrections lie in their application to a variety of wall-bounded compressible flows. The intent in this work is to develop the numerical framework for application to such flows and future work will focus on the testing of different types of models which are better posed and more suited for comparison purposes.

13

4 Numerical Implementation

In the previous sections, the mean Navier-Stokes and turbulent transport equations were developed using Cartesian tensor notation. This notation compacted the form of the equations so that the various models could be discussed with some generality. Of course the component equations need to be discretized - for a total of 7 equations for a two-equation model and 12 equations for the Reynolds stress model. It is most convenient to discuss the discretization of these equations by defining vector arrays for the dependent variables and analyzing a set of vector equations. In addition, for notational simplicity, the overbars and tildes are dropped from the mean variables with the understanding that these are Favre-averaged variables.

Expanding Eqs. (2.3), (2.4), (2.5) and the modeled forms of (2.7) and (2.9), the mean Navier-Stokes and turbulent transport equations can be written in vector form in an arbitrary coordinate system (ξ, η, ζ) as:

$$\frac{\partial \hat{Q}}{\partial t} + \frac{\partial (\hat{F} - \hat{F}_v)}{\partial \xi} + \frac{\partial (\hat{G} - \hat{G}_v)}{\partial \eta} + \frac{\partial (\hat{H} - \hat{H}_v)}{\partial \zeta} = S \tag{4.1}$$

where $\hat{Q}$ is the vector of dependent variables

$$\hat{Q} = \frac{Q}{J} = J^{-1} \begin{Bmatrix} \rho \\ \rho u \\ \rho v \\ \rho w \\ \rho E \\ \rho \tau_{xx} \\ \rho \tau_{yy} \\ \rho \tau_{zz} \\ \rho \tau_{xy} \\ \rho \tau_{xz} \\ \rho \tau_{yz} \\ \rho \epsilon \end{Bmatrix} \tag{4.1a}$$

and F, G, H are the inviscid (convective) fluxes, F_v, G_v, H_v are the viscous (diffusive) fluxes, and S represents the source terms due to production, destruction, and redistribution.

An equation of state is required to complete the system of equations. The perfect gas equation of state is used in this study:

$$p = (\gamma - 1)[\rho E - \frac{1}{2}\rho(u^2 + v^2 + w^2) - \rho k] \tag{4.2}$$

The presence of the turbulent kinetic energy term in the equation of state arises from the Favre-averaging and creates a strong coupling between the mean equations and the normal Reynolds stress components for the Reynolds stress models or the turbulent kinetic energy equation for the two-equation models.

4.1 Discretization

The semi-discrete, finite-volume form of Eq. (4.1) is written as:

$$
\begin{aligned}
(\partial \hat{Q}/\partial t)_{ijk} &+ [(\hat{F} - \hat{F}_v)\nabla\xi/J]_{i+1/2,j,k} - [(\hat{F} - \hat{F}_v)\nabla\xi/J]_{i-1/2,j,k} \\
&+ [(\hat{G} - \hat{G}_v)\nabla\eta/J]_{i,j+1/2,k} - [(\hat{G} - \hat{G}_v)\nabla\eta/J]_{i,j-1/2,k} \\
&+ [(\hat{H} - \hat{H}_v)\nabla\zeta/J]_{i,j,k+1/2} - [(\hat{H} - \hat{H}_v)\nabla\zeta/J]_{i,j,k-1/2} \\
&\qquad\qquad\qquad\qquad\qquad -(\tfrac{1}{J}S)_{ijk} = 0
\end{aligned} \tag{4.3}
$$

where the fluxes are defined at the interfaces of the computational cell bounding the cell-average value, Q_{ijk}. The definition of the numerical flux function approximating the interface flux determines the characteristics of the numerical scheme. The current emphasis is to develop a method capable of calculating high-speed flow about complex configurations. Problems of interest include separated flows, flows with large pressure gradients, and shock/boundary-layer interactions. This requires that we develop a scheme with good shock-capturing capabilities, good accuracy and general geometric capabilities.

Upwind schemes have proven reliable for calculating flows with strong shocks. Additionally, Roe's approximate Riemann solver [22] has been shown to be accurate in viscous flows [23]. Upwind schemes allow the dissipation required of shock-capturing schemes to be scaled according to each wave type recognized by the flux function, thereby minimizing the numerical dissipation. (See e.g. [24] for an excellent review of upwind differencing techniques.) The Roe approximate Riemann solver for the mean flow equations coupled with two-equation turbulence models was previously derived and reported in [5]. Section 4.2 derives the scheme for the mean flow equations coupled with a Reynolds stress turbulence model.

Second-order spatial accuracy for the inviscid terms is attained by using the MUSCL scheme of van Leer [25]. The variables interpolated are ρ, u_i, p, τ_{ij}, and ϵ. The min-mod limiter [26] is used to avoid spurious oscillations in the neighborhood of a discontinuity. Other limiters are available and will be investigated in future work to improve monotonicity and convergence behavior.

The remaining terms to be discretized are the diffusive fluxes and the source terms. Consistent with the elliptic nature of the diffusive fluxes, a finite-volume representation of a second-order accurate central-difference operator [26, 27] is employed. Derivatives required in the diffusive flux evaluation at the cell interface are approximated with Gauss's divergence theorem, integrating around an auxiliary cell centered at the interface. Flow variables required at this interface are obtained from arithmetic averaging of neighboring cell averages. Derivatives required for the source terms are also calculated using Gauss's divergence theorem by integrating around the computational cell.

To accomodate geometrically complex configurations, we implement a multi-block procedure which requires C^0 grid continuity.

15

4.2 Roe Flux-Difference Splitting

The interface flux for the finite volume formulation is calculated in each of the three coordinate directions as the solution of a locally one-dimensional Riemann problem normal to the cell interface (the so-called operator splitting approach)

$$\frac{\partial}{\partial t}\hat{Q} + \frac{\partial}{\partial n}\overline{F} = 0 \tag{4.4}$$

$$\begin{aligned}\hat{Q} = \hat{Q}_L \quad & n < 0 \\ \hat{Q} = \hat{Q}_R \quad & n > 0\end{aligned} \tag{4.4a}$$

where n is the coordinate normal to the cell interface (ξ, η or ζ) and

$$\overline{F} = \frac{|\nabla n|}{J}\left\{\begin{array}{c} \rho\overline{U} \\ \rho u\overline{U} + \hat{n}_x p \\ \rho v\overline{U} + \hat{n}_y p \\ \rho w\overline{U} + \hat{n}_z p \\ \rho\overline{U}H \\ \rho\overline{U}\tau_{xx} \\ \rho\overline{U}\tau_{yy} \\ \rho\overline{U}\tau_{zz} \\ \rho\overline{U}\tau_{xy} \\ \rho\overline{U}\tau_{xz} \\ \rho\overline{U}\tau_{yz} \\ \rho\overline{U}\epsilon \end{array}\right\} \tag{4.4b}$$

$$\overline{U} = \hat{n}_x u + \hat{n}_y v + \hat{n}_z w. \tag{4.4c}$$

The solution of the Riemann problem results in a shock wave, a contact discontinuity, and a rarefaction evolving in time at the interface (see Fig. 1). The interface flux can then be determined as the flux at the left or right state incremented by the flux differences crossed from that state to the interface. The exact solution of the Riemann problem requires an iterative procedure and is quite expensive. A cheaper alternative developed by Roe is to construct the solution to the approximate, linearized problem:

$$\frac{\partial}{\partial t}\hat{Q} + \overline{A}\frac{\partial}{\partial n}\hat{Q} = 0 \tag{4.5}$$

where the Jacobian matrix, $\overline{A} = \partial\overline{F}/\partial\hat{Q}$, is evaluated at an average state such that it satisfies the jump condition between the flux states at the right and left:

$$\overline{F}_R - \overline{F}_L = \widehat{\overline{A}}(\hat{Q}_R - \hat{Q}_L) \tag{4.6}$$

(The complete form of the Jacobian matrix and the symmetrization matrices is given in the Appendix). The Jacobian matrix, $\overline{A}$, has twelve eigenvalues, λ_i,

$$\lambda_1 = \lambda_2 = \lambda_3 = \lambda_6 \ldots \lambda_{12} = \overline{U}|\nabla n|$$

16

$$\lambda_4 = \left(\overline{U} + a\right)|\nabla n| \tag{4.7}$$

$$\lambda_5 = \left(\overline{U} - a\right)|\nabla n|.$$

The Roe averaged variables that satisfy Eq. (4.6) are

$$\hat{\rho} = \sqrt{\rho_L \rho_R} \tag{4.8a}$$

$$\hat{H} = \frac{\sqrt{\rho_L}H_L + \sqrt{\rho_R}H_R}{\sqrt{\rho_L} + \sqrt{\rho_R}} \tag{4.8b}$$

$$\hat{u} = \frac{\sqrt{\rho_L}u_L + \sqrt{\rho_R}u_R}{\sqrt{\rho_L} + \sqrt{\rho_R}} \tag{4.8c}$$

$$\hat{v} = \frac{\sqrt{\rho_L}v_L + \sqrt{\rho_R}v_R}{\sqrt{\rho_L} + \sqrt{\rho_R}} \tag{4.8d}$$

$$\hat{w} = \frac{\sqrt{\rho_L}w_L + \sqrt{\rho_R}w_R}{\sqrt{\rho_L} + \sqrt{\rho_R}} \tag{4.8e}$$

$$\hat{q}^2 = \hat{u}^2 + \hat{v}^2 + \hat{w}^2 \tag{4.8f}$$

$$\hat{a}^2 = (\gamma - 1)(\hat{H} - \hat{q}^2/2 - \hat{k}) \tag{4.8g}$$

$$\widehat{\tau_{ij}} = \frac{\sqrt{\rho_L}\tau_{ijL} + \sqrt{\rho_R}\tau_{ijR}}{\sqrt{\rho_L} + \sqrt{\rho_R}} \tag{4.8h}$$

$$\hat{k} = (\widehat{\tau_{xx}} + \widehat{\tau_{xx}} + \widehat{\tau_{xx}})/2 \tag{4.8i}$$

$$\hat{\epsilon} = \frac{\sqrt{\rho_L}\epsilon_L + \sqrt{\rho_R}\epsilon_R}{\sqrt{\rho_L} + \sqrt{\rho_R}} \tag{4.8j}$$

The interface flux can finally be written as the average of the interface flux calculated from the left state crossing negative running waves and the right state crossing positive running waves, as:

$$\overline{F}_{i+1/2} = \frac{1}{2}[\overline{F}_R + \overline{F}_L - \left|\hat{\overline{A}}\right|(\hat{Q}_R - \hat{Q}_L)] \tag{4.9}$$

This may be written in a more computationally efficient manner as

$$\overline{F}_{i+1/2} = \frac{1}{2}[\overline{F}_R + \overline{F}_L - \sum|\Delta F|] \tag{4.10}$$

where the flux differences can be derived as:

$$
\left|\Delta F_{\overline{U}}\right| = \frac{\left|\hat{\Lambda}_{\overline{U}}\right|}{J}\left[(\Delta\rho - \Delta p/\hat{a}^2)\left\{\begin{array}{c} 1 \\ \hat{u} \\ \hat{v} \\ \hat{w} \\ \hat{q}^2/2 + \hat{k} \\ \widehat{\tau_{xx}} \\ \widehat{\tau_{yy}} \\ \widehat{\tau_{zz}} \\ \widehat{\tau_{xy}} \\ \widehat{\tau_{xz}} \\ \widehat{\tau_{yz}} \\ \hat{\epsilon} \end{array}\right\} + \hat{\rho}\left\{\begin{array}{c} 0 \\ \Delta u - \hat{n}_x\Delta\overline{U} \\ \Delta v - \hat{n}_y\Delta\overline{U} \\ \Delta w - \hat{n}_z\Delta\overline{U} \\ \hat{u}\Delta u + \hat{v}\Delta v + \hat{w}\Delta w - \hat{\overline{U}}\Delta\overline{U} + \Delta k \\ \Delta\tau_{xx} \\ \Delta\tau_{yy} \\ \Delta\tau_{zz} \\ \Delta\tau_{xy} \\ \Delta\tau_{xz} \\ \Delta\tau_{yz} \\ \Delta\epsilon \end{array}\right\}\right]
$$

$$(4.10a)$$

$$
\left|\Delta F_{\overline{U}+a}\right| = \frac{\left|\hat{\Lambda}_{\overline{U}+a}\right|}{J}\frac{\Delta p + \hat{\rho}\hat{a}\Delta\overline{U}}{2\hat{a}^2}\left\{\begin{array}{c} 1 \\ \hat{u} + \hat{n}_x\hat{a} \\ \hat{v} + \hat{n}_y\hat{a} \\ \hat{w} + \hat{n}_z\hat{a} \\ \hat{H} + \hat{\overline{U}}\hat{a} \\ \widehat{\tau_{xx}} \\ \widehat{\tau_{yy}} \\ \widehat{\tau_{zz}} \\ \widehat{\tau_{xy}} \\ \widehat{\tau_{xz}} \\ \widehat{\tau_{yz}} \\ \hat{\epsilon} \end{array}\right\}
$$

$$(4.10b)$$

$$
\left|\Delta F_{\overline{U}-a}\right| = \frac{\left|\hat{\Lambda}_{\overline{U}-a}\right|}{J}\frac{\Delta p - \hat{\rho}\hat{a}\Delta\overline{U}}{2\hat{a}^2}\left\{\begin{array}{c} 1 \\ \hat{u} - \hat{n}_x\hat{a} \\ \hat{v} - \hat{n}_y\hat{a} \\ \hat{w} - \hat{n}_z\hat{a} \\ \hat{H} - \hat{\overline{U}}\hat{a} \\ \widehat{\tau_{xx}} \\ \widehat{\tau_{yy}} \\ \widehat{\tau_{zz}} \\ \widehat{\tau_{xy}} \\ \widehat{\tau_{xz}} \\ \widehat{\tau_{yz}} \\ \hat{\epsilon} \end{array}\right\}
$$

$$(4.10c)$$

with $\Delta(\cdot) = (\cdot)_R - (\cdot)_L$.

4.3 Time Integration

The conservation and transport equations given by Eq. (4.1) must be integrated in time to provide a steady-state solution. The Reynolds stress and two-equation turbulence models are known to exhibit stiff behavior, especially in the near-wall region. Therefore, an implicit time integration is used to integrate the equations. The Euler implicit time integration scheme can be written in delta form as:

$$\left[\frac{I}{J\Delta t} + \delta_\xi(A - A_v) + \delta_\eta(B - B_v) + \delta_\zeta(C - C_v) - D\right]\Delta Q = -R^n \qquad (4.11)$$

where $\Delta Q = Q^{n+1} - Q^n$ and $A = \partial\hat{F}/\partial Q, B = \partial\hat{G}/\partial Q, C = \partial\hat{H}/\partial Q, A_v = \partial\hat{F}_v/\partial Q,$ $B_v = \partial\hat{G}_v/\partial Q, C_v = \partial\hat{H}_v/\partial Q, D = \partial S/\partial Q$ are the Jacobian matrices and R^n is the steady-state residual at time n. Eq. (4.11) results in a large banded system of block matrices which must be inverted at each time step to update the solution.

The storage requirements to solve Eq. (4.11) exactly for a large three-dimensional problem are prohibitive. Therefore, an approximate solution at each time step is obtained by solving a factored form of the equation. A spatially split, approximate factorization scheme can be written as the following four sweeps (the fourth sweep is a point implicit treatment of the source terms) through the flowfield:

$$\begin{aligned}
\left[I - J\Delta t D\right]\Delta Q' &= -J\Delta t R^n \\
\left[I + J\Delta t\delta_\xi(A - A_v)\right]\Delta Q'' &= \Delta Q' \\
\left[I + J\Delta t\delta_\eta(B - B_v)\right]\Delta Q''' &= \Delta Q'' \\
\left[I + J\Delta t\delta_\zeta(C - C_v)\right]\Delta Q &= \Delta Q''' \\
Q^{n+1} &= Q^n + \Delta Q
\end{aligned} \qquad (4.12)$$

The first factor requires only a block inversion at each point in the flowfield. The three spatial factors require the inversion of a block pentadiagonal system (block 12×12 matrices for Reynolds stress models or block 7×7 matrices for two-equation models) in each of the three coordinate directions (ξ, η, ζ) as the computational stencil for the inviscid fluxes spans five cell-centers. A computational savings can be gained by treating the inviscid fluxes as first-order accurate in the implicit sweeps. This reduces the system to block tridiagonal matrices. There is no reduction in accuracy at steady-state due to the implementation in delta form. A second benefit of first-order implicit differencing of the inviscid fluxes is gained from the unconditional diagonal dominance of the first-order system.

The source terms are currently treated in a point implicit manner in the above algorithm. Recent work on approximate factorization schemes with source terms [28] recommends including the source terms in the spatial factors rather than as a separate inversion to reduce factorization error. The current scheme has been chosen to avoid storing the source Jacobian and to facilitate the implementation (at a future date) of a diagonalized version of the scheme [29].

The source term is a function of both the conserved variables and derivatives of the conserved variables, $S = S(Q, \partial Q/\partial x_i)$. For the current calculations, D is

19

simplified to include only the implicit contributions from the conserved variables in order to preserve the point implicit treatment. The inclusion of the $\partial S/\partial(\partial Q/\partial x_i)$ terms is possible in the spatially split factors, but is not included at present. The net result of neglecting the contribution due to the derivatives of the conserved variables is to essentially decouple the turbulence transport equations from the mean flow equations in the source term treatment. This is exactly what most researchers have implemented when they solve the mean flow equations coupled and then update the turbulence tranpsort equations separately. However, there is still a coupling of the normal stress components with the mean flow equations as can be seen from the Jacobian matrices.

5 Results

As mentioned previously, the intention in this report is not to evaluate turbulent closure models but to develop a numerical methodology which is capable of using either two-equation or Reynolds stress closure models in the solution of compressible flow equations. The task of evaluating closure models in an unambiguous fashion requires the use of a common numerical procedure so that any bias from the numerics can be consistently minimized. As was discussed in the previous section, there are a variety of ways of handling both the coupling of the equations and the differencing of the various terms. With the development of the technique outlined in this report, it will now be possible to evaluate a variety of closure models. This evaluation is presently just beginning and will be the subject of future reports.

In this section, the results from some initial computations using both two-equation and Reynolds stress models will be presented. These are not intended as a comparison of model performance, rather these are intended to illustrate the numerical code's capability. In fact, a fair comparison of closure models in wall-bounded compressible flows may not be possible at this time. As has been alluded to earlier, the high Reynolds number form of both two-equation and Reynolds stress models has been fairly well established, even in the compressible regime for moderately high Mach numbers. However, the development of appropriate near-wall models for these closures in order to integrate directly to the wall has not been completed, particularly in the compressible high Mach number regime. This is particularly crucial when one realizes that the stiffness problems commonly associated with the Reynolds stress models are due to an improper balance of terms in the modeled equations for the near-wall region. Another factor complicating any sensible comparison of two-equation and Reynolds stress models is the lack of experimental data. Even in cases where there are data, the data are by no means complete, that is, measurements of turbulence profiles are rare and without them any comparisons of model performance is indirectly obtained through comparisons with mean flow variables. The approach taken here is to use a variable density extension of an incompressible near-wall model and to analyze its ability to calculate the turbulent stress components. The $k - \epsilon$ version of the Speziale, Abid and Anderson model [6] will be used for the two-equation tests and the Shima model [20] will be used for the Reynolds stress test.

One test case that will be presented is the two-dimensional flow over a 10° compression ramp. The ramp flow is Mach 3 with a mean flow Reynolds number of 10×10^6 and adiabatic wall conditions. The free-stream temperature, T_∞, is set at $300°K$. The flow field will be calculated using both the two-equation and Reynolds stress models.

A second test case is the three-dimensional flow over a 5° cone at 2° angle of attack. The cone flow is Mach 3.5 with a mean flow Reynolds number of 2.21×10^7 and adiabatic wall conditions. The free-stream temperature is $311°K$. The cone flow field will be run with the two-equation model only just to validate the three-

dimensional capability of the code.

The boundary conditions for the calculations are applied explicitly. The inflow data are completely set to free-stream values for supersonic calculations. The free-stream turbulent kinetic energy level is specified as 1%, and the free-stream turbulent eddy viscosity is assumed equal to the free-stream molecular viscosity. From the free-stream value of turbulent kinetic energy and turbulent eddy viscosity, the free-stream value of solenoidal dissipation rate is obtained from Eq. (2.6a). An isotropic distribution is assumed for the normal components of the Reynolds stress tensor with the shear stress components set to zero for consistency. Outflow boundary conditions are zeroth-order extrapolations of the variables. The farfield boundary conditions for mean variables are held to free-stream values since the grid domain extends outside the bow shock of the flat-plate leading-edge (for the ramp problem) or the cone apex. Turbulence variables are obtained from zeroth-order extrapolation from the interior. This Neumann condition is used to minimize any farfield bias to the interior turbulence levels. The wall boundary conditions are specified as zero velocity ($u_i = 0$), zero Reynolds stresses ($\tau_{ij} = 0$), and adiabatic or specified wall temperature. At the wall, the pressure is extrapolated from the interior solution with a zeroth-order extrapolation, and the solenoidal dissipation rate is equated to the second derivative of the turbulent kinetic energy (a consequence of evaluating the turbulent kinetic energy equation at the wall).

The results from the ramp calculations will be shown first. The domain was discretized using a 101 by 51 mesh, with high grid clustering in the near-wall region, for both the two-equation and Reynolds stress calculations. It does not appear to be worthwhile to do grid refinement studies in the context of the present report since the closure models have not been finalized nor has a suitable (sufficiently well documented) set of test cases been chosen here. These are the topic of future research and are presently being initiated. Nevertheless, with the same grid structure, it will be possible to get a qualitative comparison of both the two-equation and Reynolds stress closures. The mean pressure and velocity, turbulent Reynolds stresses (kinetic energy) and turbulent dissipation rate variables that will be shown are all normalized by the free-stream mean pressure, free-stream mean density, free-stream mean velocity and flat-plate/ramp length.

Pressure contours for the 10° ramp using the two-equation model are shown in Fig. 2. Note that the domain shown is inclusive of the plate leading-edge (lower left corner of figure). The shock is captured very cleanly with no apparent oscillations, validating the shock capturing properties of the upwinding procedure for the coupled set of equations. The apparent thickening of the shock at the outer extent of the domain is due to the coarse grid in this region resulting from high grid stretching to provide adequate resolution in the near-wall region. The shock appears to affect the boundary layer near the start of the ramp and then has minimal direct affect farther downstream; however, as subsequent plots will show, the start of the ramp will have an affect on the flow field farther downstream along the ramp.

22

The mean velocity profiles are shown in Fig. 3. These profiles are the Favre-averaged Cartesian mean velocities $\tilde{u}_i = (\tilde{u}, \tilde{v}, 0)$, normalized by the free-stream velocity U_∞, with the domain set between $x = 0.0$ and $x = 1.0$. The start of the ramp is located at $x = 0.5$. The four stations show one set of profiles upstream of the ramp ($x = 0.396$), a second at the start of the ramp ($x = 0.499$), a third slightly downstream of the ramp ($x = 0.598$), and a fourth further downstream along the ramp ($x = 0.808$). The figure shows the dominance of the x-component of velocity over the entire range, although after the ramp, the y-component does increase significantly over its flat-plate value. At the first station, the $\tilde{v}$-velocity is essentially coincident with the vertical axis. The small backflow at the start of the ramp can be seen in the $x = 0.499$ plot.

Streamwise variation of the turbulent kinetic energy is shown in Fig. 4. The downstream development of the turbulent kinetic energy is clearly altered by the presence of the ramp. The ramp causes an increase in the turbulent energy away from the wall at the expense of the peak energy level near the wall ($x = 0.499$). Further downstream, the profile recovers and tends toward its flat-plate distribution.

Figure 5 shows the corresponding turbulent dissipation rate evolution. Once again, there is seen a significant effect on the turbulence as the flow is subjected to the compression ramp. At $x = 0.499$, the peak in the dissipation rate is shifted away from the wall and then by $x \approx 0.808$ it has recovered just as in the turbulent kinetic energy case. Unfortunately, the quantitative aspects of these results are questionable, since the dissipation rate should have its maximum value at the wall (e.g. [10]). Clearly, the model used is unable to capture this trend and needs to be improved. Such improvements are the focus of research at this time, and as these improvements in the models are developed they will be incorporated into the numerical code.

As a further validation of the code capabilities, the previous ramp flow was also computed using the Reynolds stress turbulence model of Shima [20]. The pressure contours for the flow are shown in Fig. 6. The results are qualitatively consistent with the results from the two-equation model. As was shown in the previous results, the shock itself does not affect the turbulence quantities within the boundary layer flow, but the effects of the ramp start will have an effect on the turbulence quantities both at the start as well as farther downstream along the ramp. Again the shock is captured cleanly with minimal oscillations, verifying the shock capturing capability of the scheme including Reynolds stress models. The shock thickening at the outer region of the domain is again due to grid coarseness in this region.

Mean velocity profiles are shown in Fig. 7 at the same streamwise stations shown for the two-equation model. The start of the ramp has the effect of retarding the flow near the wall, with the $\tilde{u}$ velocity profile at $x = 0.499$ showing that the flow is near incipient separation. The two-equation results did show separation at this point, but it was rather weak. Clearly, the initiation of the ramp causes a strong deceleration of the flow and this affects the turbulence at the ramp start as well as downstream. The velocity profiles computed using the Reynolds stress model are fuller than those from

the two-equation model suggesting that the predicted wall skin friction is higher. As in Fig. 3, the $\tilde{v}$-component velocity only begins to have an impact at the ramp start, and in this case the effect on the flat-plate and near the ramp start are minimal.

The turbulent kinetic energy shown in Fig. 8 is obtained from the trace of the normal stress components of the Reynolds stress tensor. The qualitative features of the profiles are similar to those obtained using the two-equation model. The effect of the ramp once again causes the turbulent kinetic energy to increase farther from the wall and then to subsequently relax back farther downstream. A comparison with the two-equation results in Fig. 4 clearly shows that the Reynolds stress closure produces a significantly smaller response to the ramp start than the two-equation closure. The difference in magnitude between the two-equation and Reynolds stress results is easily explained. In the two-equation case, the Reynolds stress components are extracted from the Boussinesq approximation which causes a 'rapid response' of the stresses to the abrupt change of geometry at the ramp start; whereas, the Reynolds stress model has inherent relaxation and memory characteristics that cause a more tempered response to such geometric changes.

Figure 9 shows the turbulent dissipation rate profiles at various streamwise stations. These results suffer from the same deficiency that the dissipation rate from the two-equation model had in that the dissipation rate does not peak at the wall. Otherwise, the trends are the same as in Fig. 5 where the ramp caused the dissipation rate to increase initially and then relax back to its flat-plate level farther downstream. In this case, the turbulent dissipation rate levels are less than the corresponding levels for the two-eqaution closure. This is, of course, consistent with trends shown for the turbulent kinetic energy.

An advantage of the Reynolds stress closure model is the ability to give the behavior of the component stresses. The normal stress components are shown in Fig. 10 where the τ_{xx}, τ_{yy} and τ_{zz} Reynolds stresses are shown. As the figure shows, the τ_{xx} and τ_{zz} components dominate in their contribution to the turbulent kinetic energy. The start of the ramp initiates a large increase in the level of component energy from the flat-plate levels, which as the kinetic energy plot shows, persists downstream to the $x = 0.598$ station. All three components show an increase in energy level over a wide region of the boundary layer at this station. This 'overshoot' has diminished somewhat by the station $x = 0.808$.

The only component of the Reynolds shear stress to survive in this two-dimensional flow is the τ_{xy} component. Figure 11 shows its variation with downstream distance. The shear stress profile is also affected by the ramp start, although not to the same extent as the other turbulence profiles. In addition, downstream of the ramp start, along the ramp, the Reynolds shear stress goes positive in the near-wall region. While some regions of positive shear stress may be expected near the point of incipient separation, the wide streamwise extent of the positive shear stress values is questionable. This widespread effect is probably due to an error in the near-wall model and/or the grid resolution in this region. Shima's Reynolds stress model was developed for

incompressible flows and may prove to be inadequate for compressible, high Mach number flow fields with a simple variable density extension. Downstream of the ramp start, the shear stress levels relax back to their flat-plate levels.

The next set of results to be shown are for the three-dimensional turbulent flow over an axisymmetric cone at angle of attack. The domain was discretized into a 49 by 65 by 25 mesh (streamwise by normal by circumferential), with high grid clustering once again near the solid surface. Three-dimensional calculations are computationally intensive and for the purposes of the present report, only a two-equation turbulent closure model was applied to this flow. The variables shown will be normalized as before in the ramp case.

Figure 12 shows the cone at angle of attack to the mean flow with pressure contours superimposed. The bow shock is again captured with no apparent oscillations. The grid has extreme resolution in the near wall region (approximately 20 grid points are within the region $y^+ < 20$), resulting in an extremely coarse grid at the outer boundary and thick bow shock. Inviscidly, this cone flow field would exhibit conical scaling, where the solution would be constant along rays eminating from the cone apex. Due to viscous effects, the flow field exhibits only quasi-conical behavior away from the cone apex, allowing us to look at a single cross-section of the calculation to gain qualitative, but not quantitative, information about the entire flow field. For this purpose, the station $x = 0.83$ (based cone length of unity), which is well downstream of the cone apex, is chosen to show the azimuthal variation of the mean and turbulent quantities.

The Cartesian mean velocity components $\tilde{u}_i = (\tilde{u}, \tilde{v}, \tilde{w})$ (scaled by the free-stream velocity) are shown in Fig. 13 at four azimuthal locations: $\phi = 86.25°$ (top, leeward side), $\phi = 26.25°$, $\phi = -26.25°$, and $\phi = -86.25°$ (bottom, windward side). The vertical coordinate is the radial distance measured from the x-axis. In all the figures, the normal and circumferential velocities have minimal effect on the total mean velocity. From the streamwise component profile, it appears that there is a strong suppression of the turbulence on the windward side of the cone where the boundary layer is quite thin. On the leeward side, a thicker boundary-layer region is present, since the layer is not being constrained by a strong impinging mean flow.

Figure 14 shows the corresponding azimuthal variation of the turbulent kinetic energy. The figure shows that the boundary layer is quite thin on both the leeward and windward sides of the cone, although the leeward side boundary layer thickness is about twice the size of the windward side. The peak turbulent intensity, which occurs very near the wall, is relatively constant over the azimuthal range of the plot.

The solenoidal turbulent dissipation rate is shown in Fig. 15. As expected, the trends are consistent with the kinetic energy profiles, with the peak dissipation rate increasing as the windward side of the cone is approached. Note that significant dissipation levels are constrained to regions very near the wall.

6 Concluding Remarks

The purpose of this report is to establish both the differential and numerical framework for the development of a numerical algorithm for the solution of compressible turbulent flow problems with both two-equation and Reynolds stress turbulence closure models. As the report has shown, the task is straightforward, but rather cumbersome. There are a significant number of unknown correlations which need to be modeled and which have not received sufficient attention by the scientific community to be adequately validated. This validation process, however, can only be accomplished by the development of the type of numerical code outlined here. With the present tool, a variety of complex flows can be examined using both the two-equation and Reynolds stress closure models with the dual goal of developing better closure models and comparing the predictive capabilities of both two-equation and Reynolds stress formulations.

The test problems that were computed here were chosen to show the capabilities of the code rather than to compare the models used. If a formal comparison were intended, improved closure models would need to be used. Nevertheless, even with this type of qualitative study, results were obtained for both the ramp and cone problems which showed some interesting chararcteristic features of the mean and turbulent flow field. Unfortunately, a more thorough study is rather computationally costly and should only be performed after the methodology is validated. Work is beginning on this next phase of research where improved versions of the two-equation and Reynolds stress models will be implemented into the code which will be used for predicting selected flow problems.

Acknowledgments

Appendix

The Jacobian matrices, (A, B, C), may be written for $n = (\xi, \eta, \zeta)$ as:

$$\frac{\partial \overline{F}}{\partial \overline{Q}} = |\nabla n| \begin{bmatrix}
0 & \hat{n}_x & \hat{n}_y & \hat{n}_z & 0 & 0 & 0 & 0 & 0 & 0 & 0 & 0 \\
\hat{n}_x\Phi - u\overline{U} & \overline{U} - \hat{n}_x(\gamma-2)u & \hat{n}_y u - \hat{n}_x(\gamma-1)v & \hat{n}_z u - \hat{n}_x(\gamma-1)w & \hat{n}_x(\gamma-1) & -\hat{n}_x(\gamma-1)/2 & -\hat{n}_x(\gamma-1)/2 & -\hat{n}_x(\gamma-1)/2 & 0 & 0 & 0 & 0 \\
\hat{n}_y\Phi - v\overline{U} & \hat{n}_x v - \hat{n}_y(\gamma-1)u & \overline{U} - \hat{n}_y(\gamma-2)v & \hat{n}_z v - \hat{n}_y(\gamma-1)w & \hat{n}_y(\gamma-1) & -\hat{n}_y(\gamma-1)/2 & -\hat{n}_y(\gamma-1)/2 & -\hat{n}_y(\gamma-1)/2 & 0 & 0 & 0 & 0 \\
\hat{n}_z\Phi - w\overline{U} & \hat{n}_x w - \hat{n}_z(\gamma-1)u & \hat{n}_y w - \hat{n}_z(\gamma-1)v & \overline{U} - \hat{n}_z(\gamma-2)w & \hat{n}_z(\gamma-1) & -\hat{n}_z(\gamma-1)/2 & -\hat{n}_z(\gamma-1)/2 & -\hat{n}_z(\gamma-1)/2 & 0 & 0 & 0 & 0 \\
\overline{U}\Phi - \overline{U}H & \hat{n}_x H - (\gamma-1)u\overline{U} & \hat{n}_y H - (\gamma-1)v\overline{U} & \hat{n}_z H - (\gamma-1)w\overline{U} & \gamma\overline{U} & -(\gamma-1)\overline{U}/2 & -(\gamma-1)\overline{U}/2 & -(\gamma-1)\overline{U}/2 & 0 & 0 & 0 & 0 \\
-\overline{U}\tau_{xx} & \hat{n}_x\tau_{xx} & \hat{n}_y\tau_{xx} & \hat{n}_z\tau_{xx} & 0 & \overline{U} & 0 & 0 & 0 & 0 & 0 & 0 \\
-\overline{U}\tau_{yy} & \hat{n}_x\tau_{yy} & \hat{n}_y\tau_{yy} & \hat{n}_z\tau_{yy} & 0 & 0 & \overline{U} & 0 & 0 & 0 & 0 & 0 \\
-\overline{U}\tau_{zz} & \hat{n}_x\tau_{zz} & \hat{n}_y\tau_{zz} & \hat{n}_z\tau_{zz} & 0 & 0 & 0 & \overline{U} & 0 & 0 & 0 & 0 \\
-\overline{U}\tau_{xy} & \hat{n}_x\tau_{xy} & \hat{n}_y\tau_{xy} & \hat{n}_z\tau_{xy} & 0 & 0 & 0 & 0 & \overline{U} & 0 & 0 & 0 \\
-\overline{U}\tau_{xz} & \hat{n}_x\tau_{xz} & \hat{n}_y\tau_{xz} & \hat{n}_z\tau_{xz} & 0 & 0 & 0 & 0 & 0 & \overline{U} & 0 & 0 \\
-\overline{U}\tau_{yz} & \hat{n}_x\tau_{yz} & \hat{n}_y\tau_{yz} & \hat{n}_z\tau_{yz} & 0 & 0 & 0 & 0 & 0 & 0 & \overline{U} & 0 \\
-\overline{U}\epsilon & \hat{n}_x\epsilon & \hat{n}_y\epsilon & \hat{n}_z\epsilon & 0 & 0 & 0 & 0 & 0 & 0 & 0 & \overline{U}
\end{bmatrix}$$

where

$$\overline{U} = \hat{n}_x u + \hat{n}_y v + \hat{n}_z w$$

$$\Phi = \tfrac{1}{2}(\gamma - 1)q^2$$

The Jacobian matrix may be written as $\frac{\partial \overline{F}}{\partial \overline{Q}} = T\Lambda T^{-1}$. The symmetry matrix, T, is given as:

$$
T = \begin{bmatrix}
1 & 0 & 0 & 1 & 1 & 0 & 0 & 0 & 0 & 0 & 0 & 0 \\
u & \hat{l}_x & \hat{m}_x & u+\hat{n}_x a & u-\hat{n}_x a & 0 & 0 & 0 & 0 & 0 & 0 & 0 \\
v & \hat{l}_y & \hat{m}_y & v+\hat{n}_y a & v-\hat{n}_y a & 0 & 0 & 0 & 0 & 0 & 0 & 0 \\
w & \hat{l}_z & \hat{m}_z & w+\hat{n}_z a & w-\hat{n}_z a & 0 & 0 & 0 & 0 & 0 & 0 & 0 \\
q^2/2+k & \overline{V} & \overline{W} & H+\overline{U}a & H-\overline{U}a & 1/2 & 1/2 & 1/2 & 0 & 0 & 0 & 0 \\
\tau_{xx} & 0 & 0 & \tau_{xx} & \tau_{xx} & 1 & 0 & 0 & 0 & 0 & 0 & 0 \\
\tau_{yy} & 0 & 0 & \tau_{yy} & \tau_{yy} & 0 & 1 & 0 & 0 & 0 & 0 & 0 \\
\tau_{zz} & 0 & 0 & \tau_{zz} & \tau_{zz} & 0 & 0 & 1 & 0 & 0 & 0 & 0 \\
\tau_{xy} & 0 & 0 & \tau_{xy} & \tau_{xy} & 0 & 0 & 0 & 1 & 0 & 0 & 0 \\
\tau_{xz} & 0 & 0 & \tau_{xz} & \tau_{xz} & 0 & 0 & 0 & 0 & 1 & 0 & 0 \\
\tau_{yz} & 0 & 0 & \tau_{yz} & \tau_{yz} & 0 & 0 & 0 & 0 & 0 & 1 & 0 \\
\epsilon & 0 & 0 & \epsilon & \epsilon & 0 & 0 & 0 & 0 & 0 & 0 & 1
\end{bmatrix}
$$

where

$$\overline{V} = \hat{l}_x u + \hat{l}_y v + \hat{l}_z w$$

$$\overline{W} = \hat{m}_x u + \hat{m}_y v + \hat{m}_z w$$

The inverse of the symmetry matrix, T^{-1}, is given as:

$$
\mathbf{T^{-1}} =
\begin{bmatrix}
1-\Upsilon q^2/2 & \Upsilon u & \Upsilon v & \Upsilon w & -\Upsilon & \Upsilon/2 & \Upsilon/2 & \Upsilon/2 & 0 & 0 & 0 & 0 \\
-\overline{V} & \hat{l}_x & \hat{l}_y & \hat{l}_z & 0 & 0 & 0 & 0 & 0 & 0 & 0 & 0 \\
-\overline{W} & \hat{m}_x & \hat{m}_y & \hat{m}_z & 0 & 0 & 0 & 0 & 0 & 0 & 0 & 0 \\
\Upsilon q^2/4-\overline{U}/2a & \hat{n}_x/2a-\Upsilon u/2 & \hat{n}_y/2a-\Upsilon v/2 & \hat{n}_z/2a-\Upsilon w/2 & \Upsilon/2 & -\Upsilon/4 & -\Upsilon/4 & -\Upsilon/4 & 0 & 0 & 0 & 0 \\
\Upsilon q^2/4+\overline{U}/2a & -\hat{n}_x/2a-\Upsilon u/2 & -\hat{n}_y/2a-\Upsilon v/2 & -\hat{n}_z/2a-\Upsilon w/2 & \Upsilon/2 & -\Upsilon/4 & -\Upsilon/4 & -\Upsilon/4 & 0 & 0 & 0 & 0 \\
-\tau_{xx} & 0 & 0 & 0 & 0 & 1 & 0 & 0 & 0 & 0 & 0 & 0 \\
-\tau_{yy} & 0 & 0 & 0 & 0 & 0 & 1 & 0 & 0 & 0 & 0 & 0 \\
-\tau_{zz} & 0 & 0 & 0 & 0 & 0 & 0 & 1 & 0 & 0 & 0 & 0 \\
-\tau_{xy} & 0 & 0 & 0 & 0 & 0 & 0 & 0 & 1 & 0 & 0 & 0 \\
-\tau_{xz} & 0 & 0 & 0 & 0 & 0 & 0 & 0 & 0 & 1 & 0 & 0 \\
-\tau_{yz} & 0 & 0 & 0 & 0 & 0 & 0 & 0 & 0 & 0 & 1 & 0 \\
-\epsilon & 0 & 0 & 0 & 0 & 0 & 0 & 0 & 0 & 0 & 0 & 1
\end{bmatrix}
$$

where

$$\Upsilon = (\gamma-1)/a^2$$

The vectors $\hat{l}$ and $\hat{m}$ are non-unique, mutually orthogonal to n, and tangent vectors in the plane of the cell interface. The flux differences given in Section 4 use metric identities to provide a form which is independent of these tangency vectors for computational efficiency.

References

[1] Reynolds, W.C., "The Potential and Limitations of Direct and Large Eddy Simulations," *Proc. Whither Turbulence Workshop, Ithaca, NY Lecture Notes in Physics*, (ed.) J. L. Lumley, Berlin: Springer-Verlag, pp. 313-342, 1989.

[2] Sarkar, S., Erlebacher, G., and Hussaini, M.Y., "Direct Simulation of Compressible Turbulence in a Shear Flow," *Theoret. Comput. Fluid Dynamics*, Vol. 2, Number 5/6, pp. 291-306, 1991.

[3] Favre, A., "Equations des Gaz Turbulents Compressibles," *J. Mecanique*, Vol. 4, No. 3, pp. 361-390, 1965.

[4] Favre, A., "Formulation of the Statistical Equations of Turbulent Flows with Variable Density," *Studies in Turbulence*, (eds.) T.B. Gatski, S. Sarkar, C.G. Speziale, New York, Springer-Verlag, pp. 324-341, 1991.

[5] Morrison, J. H., "Flux-Difference Split Scheme for Turbulent Transport Equations," *AIAA 2nd International Aerospace Planes Conference*, October 29-31, Orlando, Florida, Paper No. 90-5251, 1990.

[6] Speziale, C.G., Abid, R., and Anderson, E.C., "A Critical Evaluation of Two-Equation Models for Near-Wall Turbulence," *AIAA 21st Fluid Dynamics, Plasma Dynamics and Lasers Conference*, Paper No. 90-1481, June 18-20, Seattle, WA, 1990.

[7] Reynolds, W. C., "Recent Advances in the Computation of Turbulent Flows," *Adv. Chem. Eng.*, Vol. 9, pp. 193 - 246, 1974.

[8] Zeman, O., "Dilatation Dissipation: The Concept and Application in Modeling Compressible Mixing Layers," *Phys. Fluids A*, Vol. 2, No. 2, pp. 178-188, 1990.

[9] Sarkar, S., Erlebacher, G., Hussaini, M.Y., and Kreiss, H.O., "The Analysis and Modelling of Dilatational Terms in Compressible Turbulence," *J. Fluid Mech.*, Vol. 227, pp. 473-493, 1991.

[10] Zhang, H.S., So, R.M.C., Speziale, C.G. and Lai, Y.G., "A Near-Wall Two-Equation Model for Compressible Turbulent Flows," *AIAA 30th Aerospace Sciences Meeting*, Paper No. 92-0442, January 6-9, Reno, Nevada, 1992.

[11] Launder, B.E., Reece, G.J., and Rodi, W., "Progress in the Development of a Reynolds-Stress Turbulence Closure," *J. Fluid Mech.*, Vol. 68, pp. 537-566, 1975.

[12] Sarkar, S., "Modeling the Pressure-Dilatation Correlation Term," *ICASE Report No. 91-42*, May, 1991.

[13] Zeman, O., "On the Decay of Compressible Isotropic Turbulence," *Phys. Fluids A*, Vol. 3, No. 5, pp. 951-955, 1991.

[14] Speziale, C.G., Sarkar, S., and Gatski, T.B., "Modelling the Pressure-Strain Correlation of Turbulence: An Invariant Dynamical Systems Approach," it J. Fluid Mech., Vol. 227, pp. 245-272, 1991.

[15] Speziale, C.G. and Sarkar, S., "Second-Order Closure Models for Supersonic Turbulent Flows," *AIAA 29th Aerospace Sciences Meeting*, Paper No. 91-0217, January 7-10, Reno, Nevada, 1991.

[16] Coleman, G.N. and Mansour N.N., "Simulation and Modeling of Homogeneous Compressible Turbulence under Isotropic Mean Compression," *Proceedings of Eight Symposium on Turbulent Shear Flows*, Paper No. 21-3, Technical University of Munich, September 9-11, 1991.

[17] Patel, V.C., Rodi, W. and Scheuer, G., "Turbulence Models for Near-Wall and Low-Reynolds Number Flows: A Review," *AIAA Journal*, Vol. 23, pp. 1308-1319, 1985.

[18] So, R.M.C., Lai, Y.G., Zhang, H.S., and Hwang, B.C., "A Review of Near-Wall Reynolds-Stress Closures," *NASA Contractor Report 4369*, May, 1991.

[19] Gatski, T.B. and Glauser, M.N., "Proper Orthogonal Decomposition Based Turbulence Modeling," *ICASE/LaRC Workshop on Transition and Turbulence*, July 8 - August 2, 1991.

[20] Shima, N., "A Reynolds-Stress Model for Near-Wall and Low-Reynolds -Number Regions," *Transactions of the ASME*, Vol. 110, pp. 38-44, 1988.

[21] Launder, B.E., and Shima, N., "Second-Moment Closure for the Near-Wall Sublayer: Development and Applications," *AIAA J.*, Vol. 27, No. 10, pp. 1319-1325, 1989.

[22] Roe, P. L., "Approximate Riemann Solvers, Parameter Vectors, and Difference Schemes", *Journal of Computational Physics*, Vol. 43, pp. 357-372, 1981.

[23] van Leer, B., Thomas, J. L., Roe, P. L., and Newsome, R. W., "A Comparison of Numerical Flux Formulas for the Euler and Navier-Stokes Equations," *AIAA 8th Computational Fluid Dynamics Conference*, Paper No. 87-1104, June 9-11, Honolulu, Hawaii, 1987.

[24] Walters, R. W., and Thomas, J. L., Advances in Upwind Relaxation Methods, *State-of-the-Art Surveys on Computational Mechanics*, (ed.) A.K. Noor, ASME New York, pp. 145-183, 1989.

[25] van Leer, B., "Towards the Ultimate Conservative Difference Schemes V. A Second Order Sequel to Godunov's Method", *J. Comp. Physics*, Vol. 32, pp. 101-136,1979.

[26] Chakravarthy, S. R., Szema, K-Y., Goldberg, U. C. and Gorski, J. J., "Application of a New Class of High Accuracy TVD Schemes to the Navier-Stokes Equations," *AIAA 23th Aerospace Sciences Meeting*, Paper No. 85-0165, January 14-17, Reno, Nevada, 1985.

[27] Swanson, R. C., and Turkel, E., "A Multistage Time-Stepping Scheme for the Navier-Stokes Equations," *AIAA 24th Aerospace Sciences Meeting*, Paper No. 85-0035, January 14-17, Reno, Nevada, 1985.

[28] Shih, T. I.-P. and Chyu, W. J., "Approximate Factorization with Source Terms", AIAA Journal, Vol. 29, No. 10, October 1991, pp. 1759-1760.

[29] Pulliam, T.H., and Steger, J.L.: "Recent Improvements in Efficiency, Accuracy, and Convergence for Implicit Approximate Factorization Algorithms," *AIAA 23th Aerospace Sciences Meeting*, Paper No. 85-0360, January 14-17, Reno, Nevada, 1985.
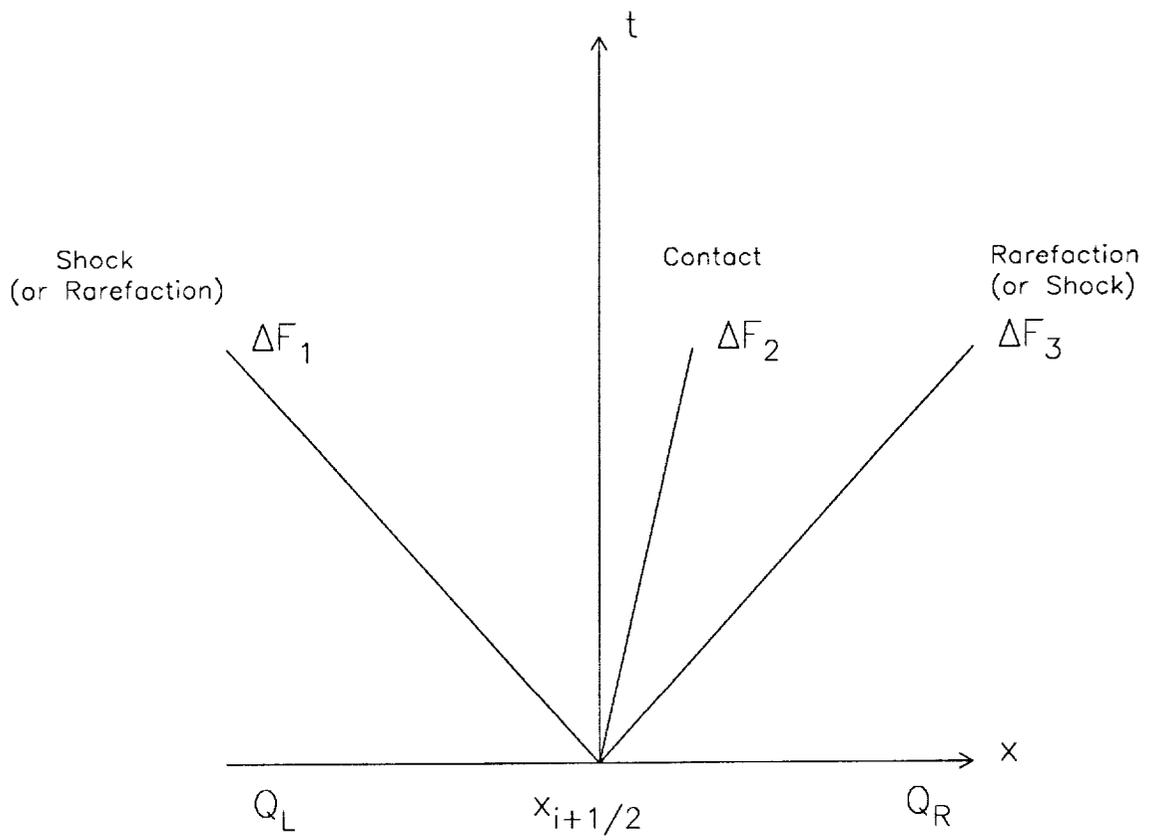
Figure 1: Diagram of shock and rarefaction wave solution to Riemann problem.
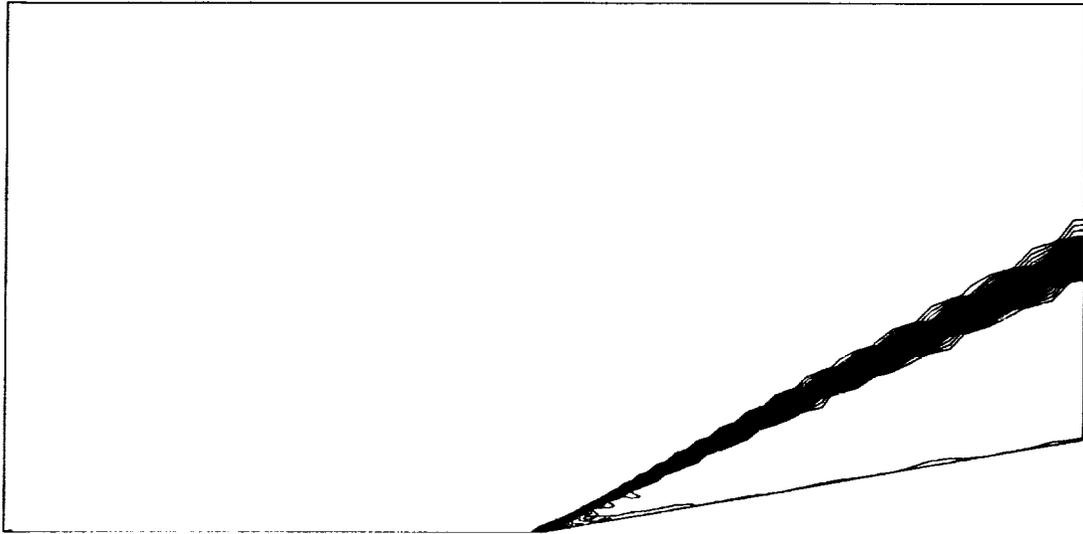
Figure 2: Pressure contours for Mach 3, 10° compression ramp using a two-equation turbulence model.
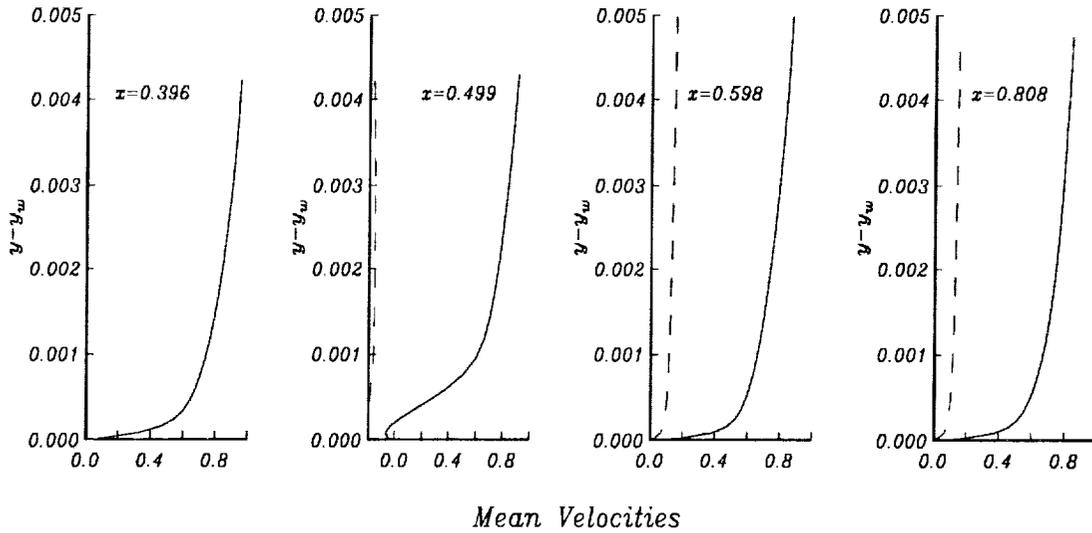
Mean Velocities

Figure 3: Streamwise variation of mean velocity profiles for 10° compression ramp using a two-equation turbulence model: $\tilde{u}/U_\infty$, ——; $\tilde{v}/U_\infty$, — —.
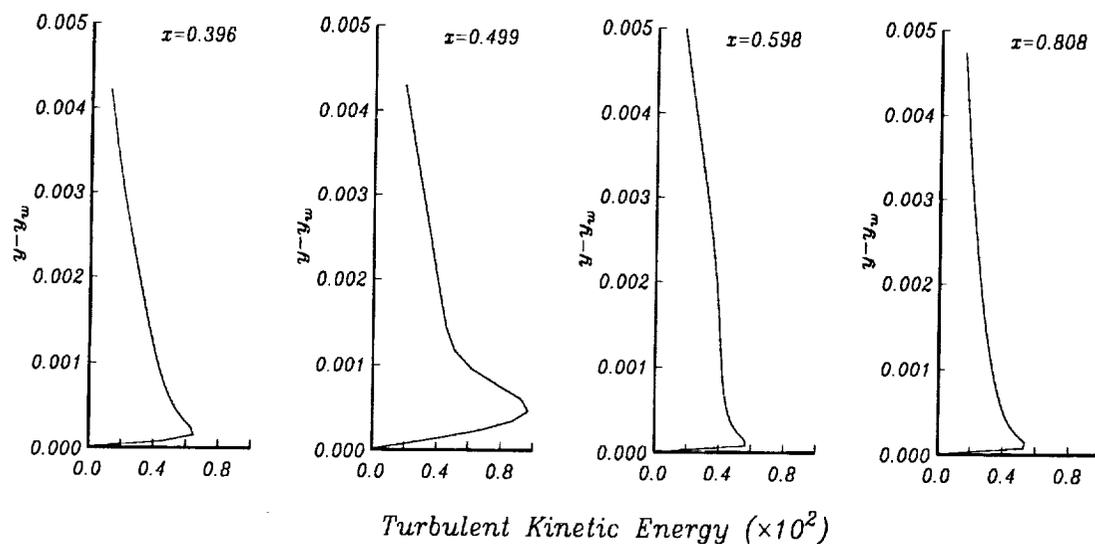
Figure 4: Streamwise variation of turbulent kinetic energy profiles for 10° compression ramp using a two-equation turbulence model.
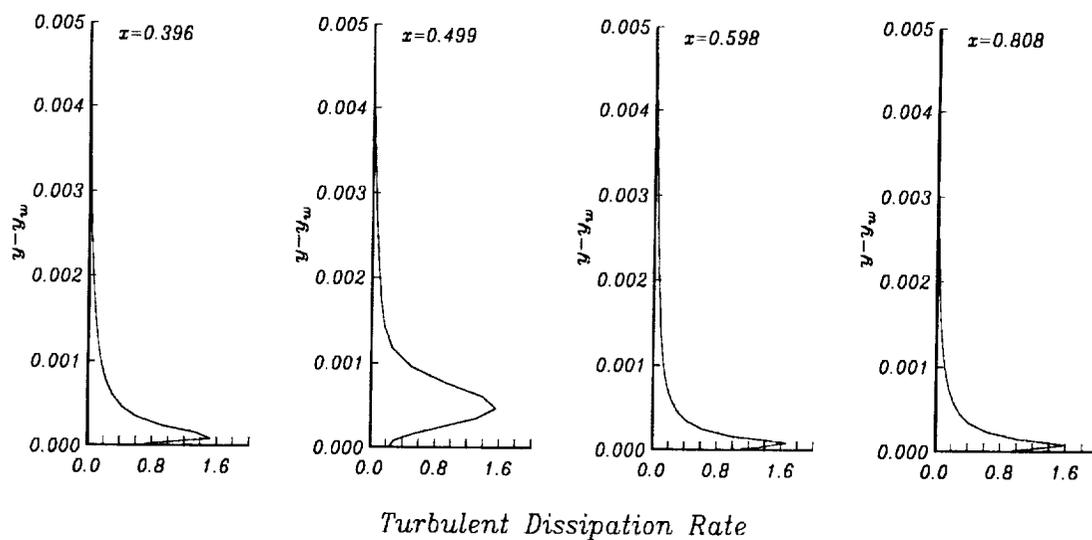

Figure 5: Streamwise variation of turbulent dissipation rate profiles for 10° compression ramp using a two-equation turbulence model.

35
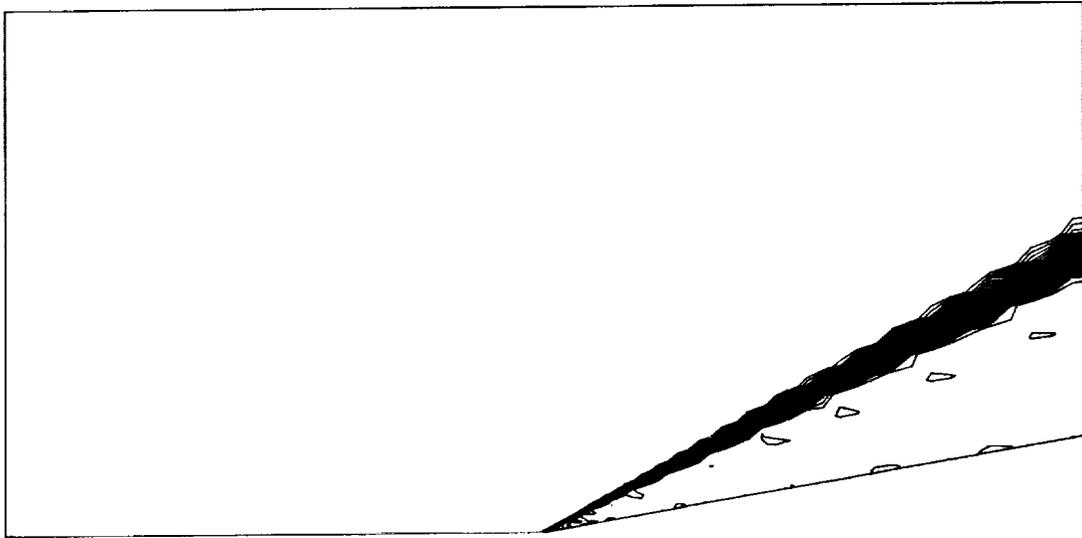
Figure 6: Pressure contours for Mach 3, 10° compression ramp using a Reynolds stress turbulence model.
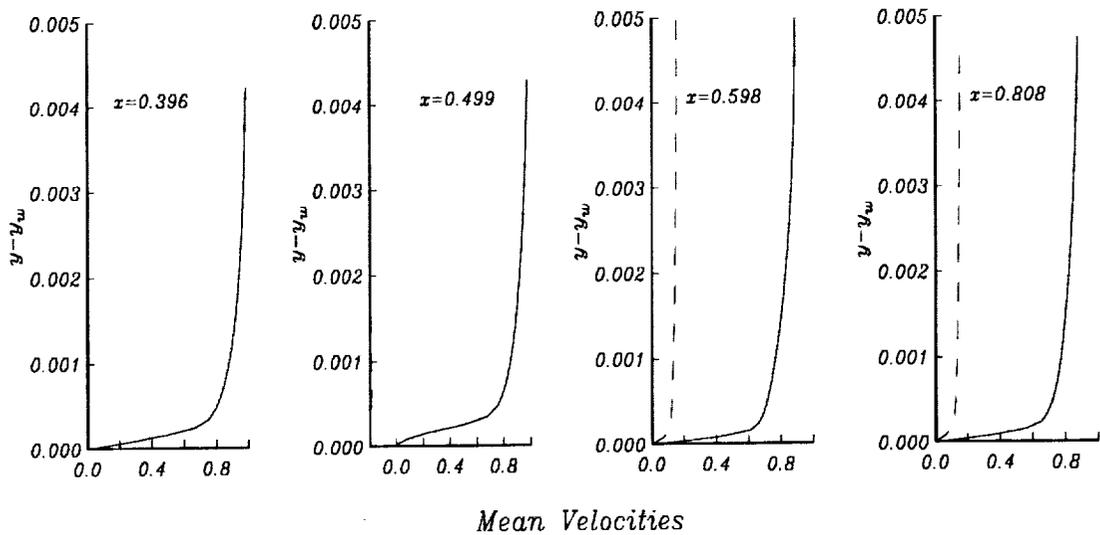
Mean Velocities

Figure 7: Streamwise variation of mean velocity profiles for 10° compression ramp using a Reynolds stress turbulence model: $\tilde{u}/U_\infty$, ——; $\tilde{v}/U_\infty$, — —.
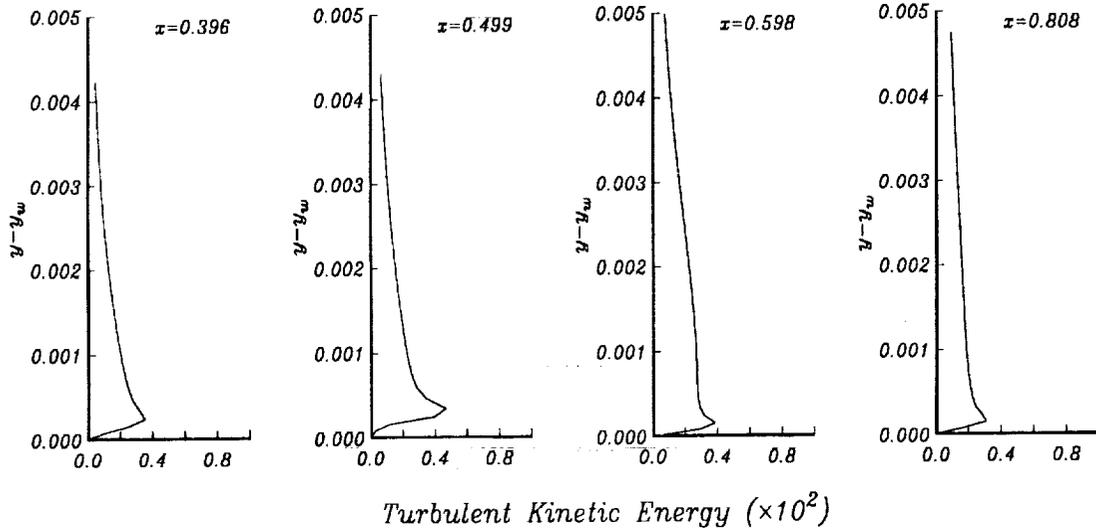
Figure 8: Streamwise variation of turbulent kinetic energy profiles for 10° compression ramp using a Reynolds stress turbulence model.
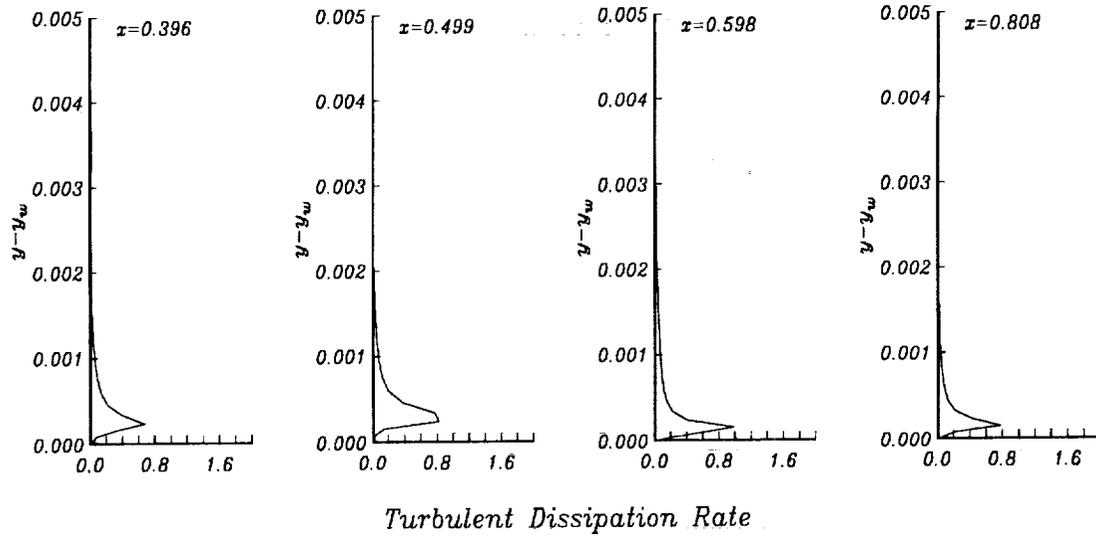
Figure 9: Streamwise variation of turbulent dissipation rate profiles for 10° compression ramp using a Reynolds stress turbulence model.
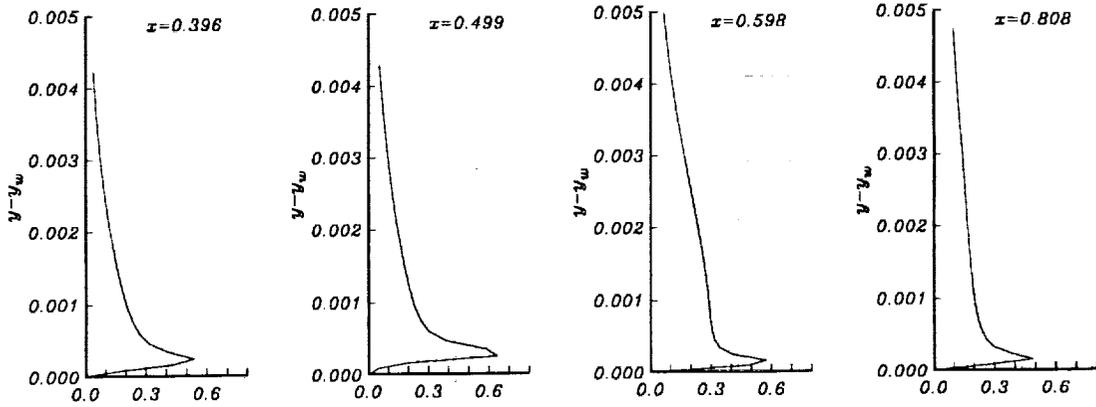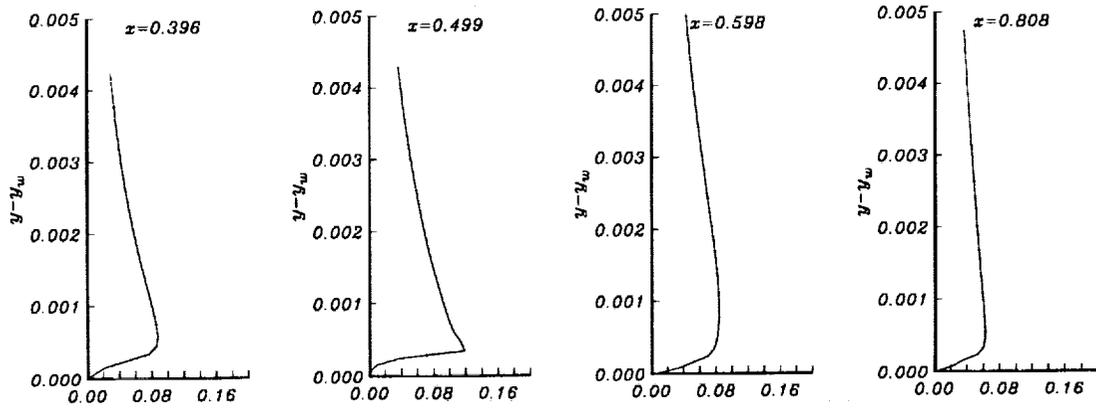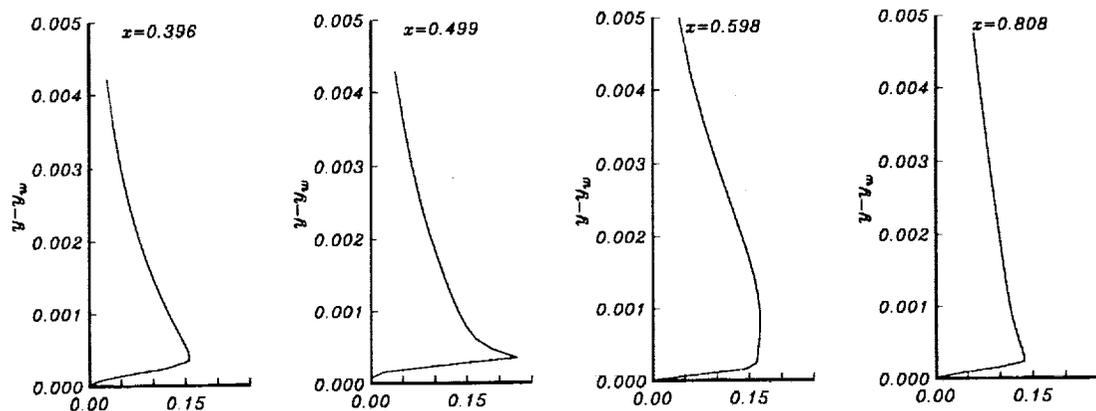
Figure 10: Normal Reynolds stress component profiles for 10° compression ramp.
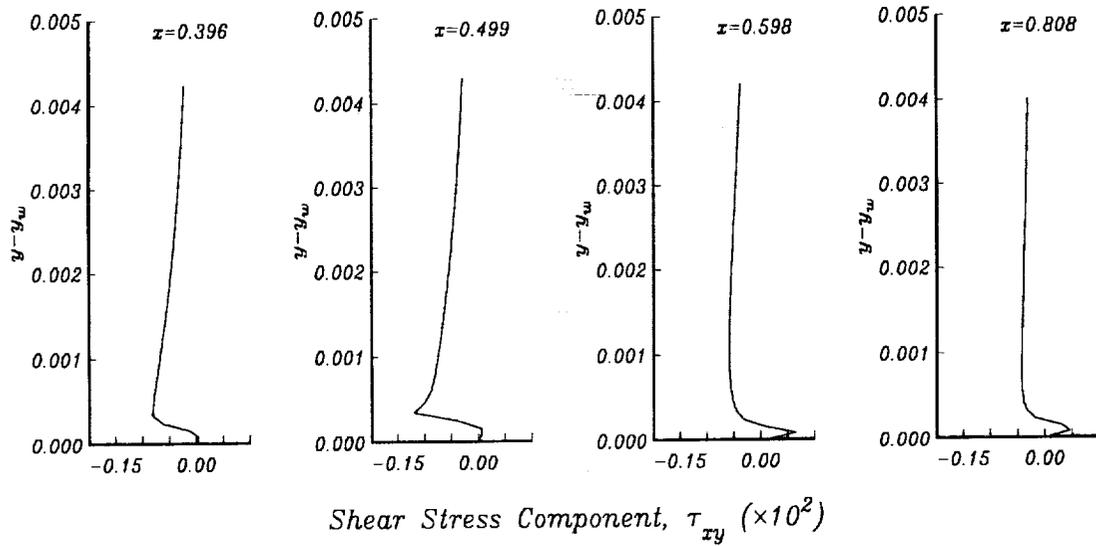
Figure 11: Reynolds shear stress profiles for 10° compression ramp.
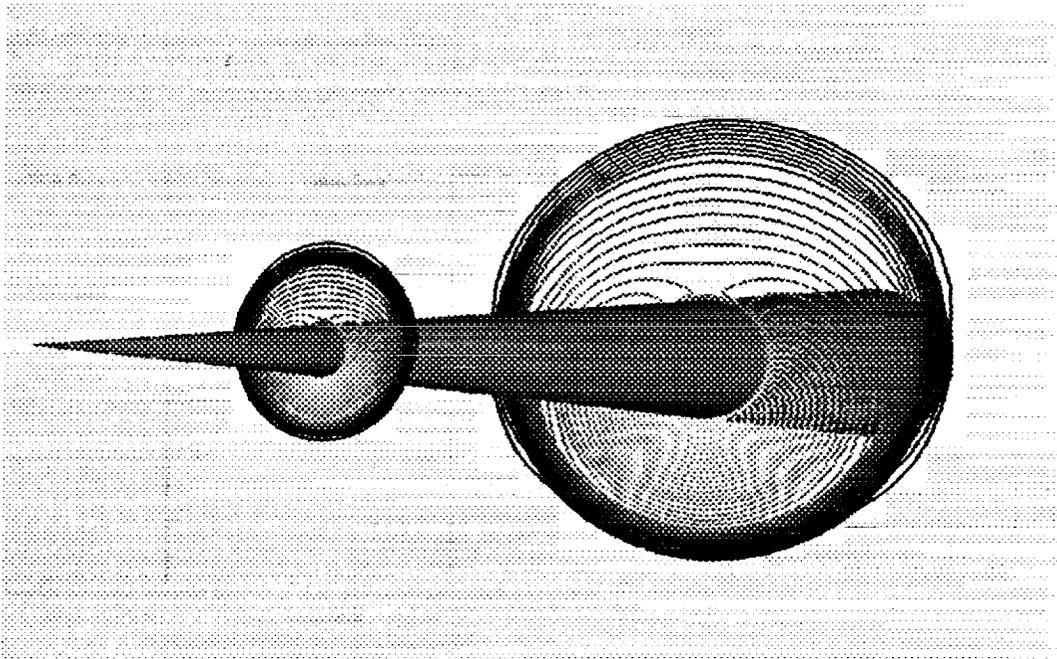
Figure 12: Pressure contours for Mach 3.5, 5° cone at 2° angle of attack using a two-equation turbulence model.
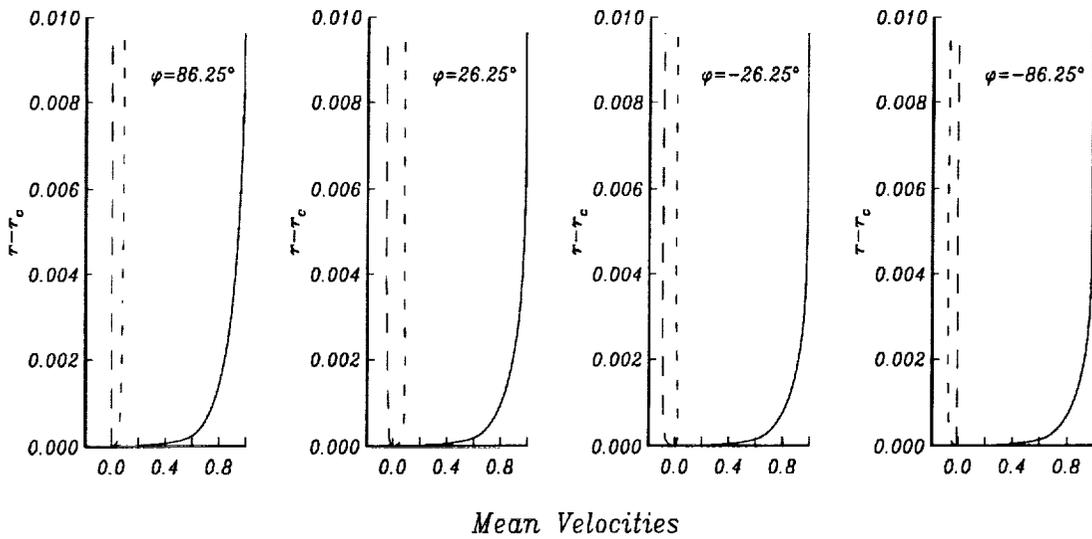
Mean Velocities

Figure 13: Azimuthal variation of mean velocities for 5° cone at 2° angle of attack using a two-equation turbulence model: $\tilde{u}/U_\infty$, ———; $\tilde{v}/U_\infty$, — —; $\tilde{w}/U_\infty$, - - -.

40
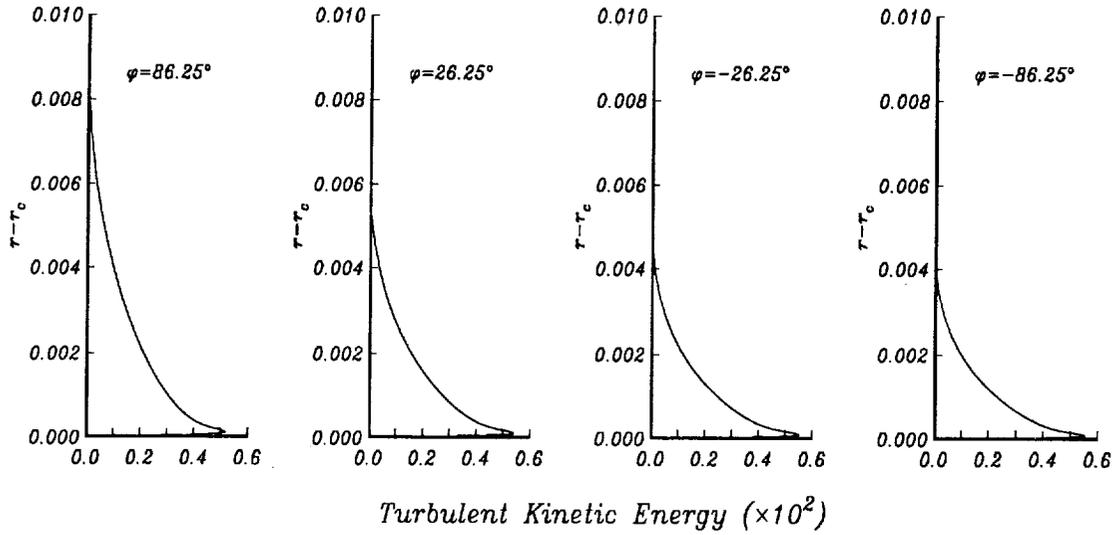
Figure 14: Azimuthal variation of turbulent kinetic energy for 5° cone at 2° angle of attack using a two-equation turbulence model.
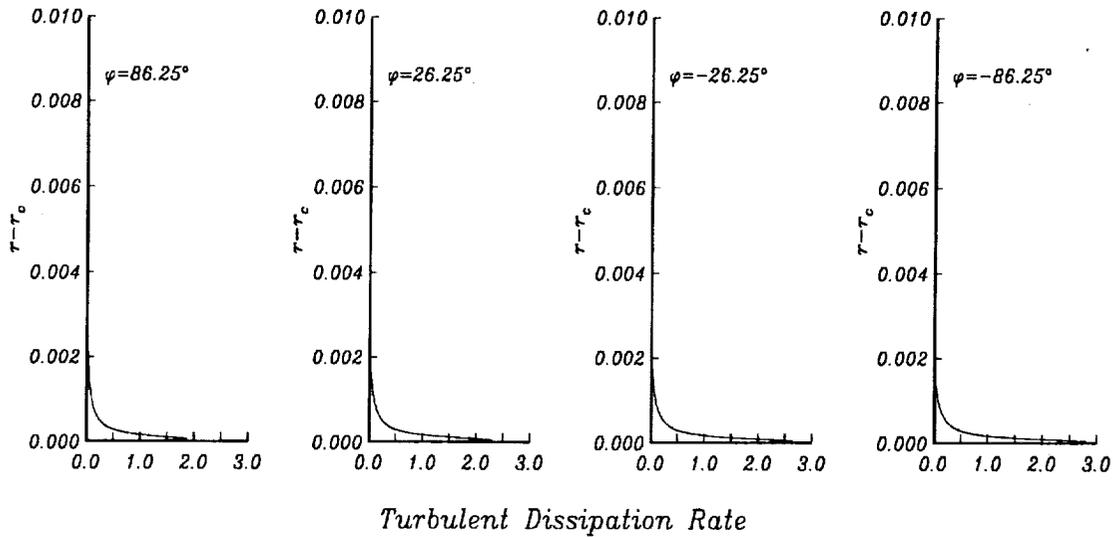

Figure 15: Azimuthal variation of turbulent dissipation rate for 5° cone at 2° angle of attack using a two-equation turbulence model.

REPORT DOCUMENTATION PAGE

Public reporting burden for this collection of information is estimated to average 1 hour per response, including the time for reviewing instructions, searching existing data sources, gathering and maintaining the data needed, and completing and reviewing the collection of information. Send comments regarding this burden estimate or any other aspect of this collection of information, including suggestions for reducing this burden, to Washington Headquarters Services, Directorate for Information Operations and Reports, 1215 Jefferson Davis Highway, Suite 1204, Arlington, VA 22202-4302, and to the Office of Management and Budget, Paperwork Reduction Project (0704-0188), Washington, DC 20503.

1. AGENCY USE ONLY (Leave blank)	2. REPORT DATE	3. REPORT TYPE AND DATES COVERED
	May 1992	Contractor Report

4. TITLE AND SUBTITLE

A Compressible Navier-Stokes Solver With Two-Equation and Reynolds Stress Turbulence Closure Models

6. AUTHOR(S)

Joseph H. Morrison

5. FUNDING NUMBERS

C NAS1-19320

WU 505-59-50-01

7. PERFORMING ORGANIZATION NAME(S) AND ADDRESS(ES)

Analytical Services & Materials, Inc.
107 Research Drive
Hampton, VA 23666

8. PERFORMING ORGANIZATION REPORT NUMBER

9. SPONSORING / MONITORING AGENCY NAME(S) AND ADDRESS(ES)

NATIONAL AERONAUTICS AND SPACE ADMINISTRATION
Langley Research Center
Hampton, VA 23665-5225

10. SPONSORING / MONITORING AGENCY REPORT NUMBER

NASA CR-4440

11. SUPPLEMENTARY NOTES

Langley Technical Monitor: Dr. Thomas B. Gatski

12a. DISTRIBUTION / AVAILABILITY STATEMENT

Unclassified - Unlimited
Subject Category - 34

12b. DISTRIBUTION CODE

13. ABSTRACT (Maximum 200 words)

This report outlines the development of a general purpose aerodynamic solver for compressible turbulent flows. Turbulent closure is achieved using either two-equation or Reynolds stress transport equations. The applicable equation set consists of Favre-averaged conservation equations for the mass, momentum and total energy, and transport equations for the turbulent stresses and turbulent dissipation rate. In order to develop a scheme with good shock-capturing capabilities, good accuracy and general geometric capabilities, a multi-block, cell-centered finite-volume approach is used. A Roe flux-difference splitting technique, coupled with a MUSCL scheme, is applied to the system of conservation and transport equations. Viscous fluxes are discretized using a finite-volume representation of a central-difference operator and the source terms are treated as an integral over the control-volume. The methodology is validated by testing the algorithm on both two-dimensional and three-dimensional flows. Both the two-equation and Reynolds stress models are used on a two-dimensional 10° compression ramp at Mach 3, and the two-equation model is used on the three-dimensional flow over a cone at angle of attack at Mach 3.5. With the development of this algorithm, it is now possible to compute complex, compressible high-speed flow fields using both two-equation and Reynolds stress turbulent closure models, with the capability of eventually evaluating their predictive performance.

14. SUBJECT TERMS	15. NUMBER OF PAGES
Navier-Stoke Solver Turbulence Modeling Compressible Turbulent Flows	44
	16. PRICE CODE A03

17. SECURITY CLASSIFICATION OF REPORT	18. SECURITY CLASSIFICATION OF THIS PAGE	19. SECURITY CLASSIFICATION OF ABSTRACT	20. LIMITATION OF ABSTRACT
Unclassified	Unclassified		